Biophysical Journal
Article

Biophysical Society

Voltage-Dependent Profile Structures of a Kv-Channel via Time-Resolved Neutron Interferometry

Andrey Y. Tronin,[1] Lina J. Maciunas,[2] Kimberly C. Grasty,[2] Patrick J. Loll,[2] Haile A. Ambaye,[3] Andre A. Parizzi,[3] Valeria Lauter,[3] Andrew D. Geragotelis,[4] J. Alfredo Freites,[4] Douglas J. Tobias,[4] and J. Kent Blasie[1,*]
[1]Department of Chemistry, University of Pennsylvania, Philadelphia, Pennsylvania; [2]Department of Biochemistry and Molecular Biology, Drexel University College of Medicine, Philadelphia, Pennsylvania; [3]Neutron Scattering Division, Neutron Sciences Directorate, Oak Ridge National Laboratory, Oak Ridge, Tennessee; and [4]Department of Chemistry, University of California Irvine, Irvine, California

ABSTRACT Available experimental techniques cannot determine high-resolution three-dimensional structures of membrane proteins under a transmembrane voltage. Hence, the mechanism by which voltage-gated cation channels couple conformational changes within the four voltage sensor domains, in response to either depolarizing or polarizing transmembrane voltages, to opening or closing of the pore domain's ion channel remains unresolved. Single-membrane specimens, composed of a phospholipid bilayer containing a vectorially oriented voltage-gated K^+ channel protein at high in-plane density tethered to the surface of an inorganic multilayer substrate, were developed to allow the application of transmembrane voltages in an electrochemical cell. Time-resolved neutron reflectivity experiments, enhanced by interferometry enabled by the multilayer substrate, were employed to provide directly the low-resolution profile structures of the membrane containing the vectorially oriented voltage-gated K^+ channel for the activated, open and deactivated, closed states of the channel under depolarizing and hyperpolarizing transmembrane voltages applied cyclically. The profile structures of these single membranes were dominated by the voltage-gated K^+ channel protein because of the high in-plane density. Importantly, the use of neutrons allowed the determination of the voltage-dependent changes in both the profile structure of the membrane and the distribution of water within the profile structure. These two key experimental results were then compared to those predicted by three computational modeling approaches for the activated, open and deactivated, closed states of three different voltage-gated K^+ channels in hydrated phospholipid bilayer membrane environments. Of the three modeling approaches investigated, only one state-of-the-art molecular dynamics simulation that directly predicted the response of a voltage-gated K^+ channel within a phospholipid bilayer membrane to applied transmembrane voltages by utilizing very long trajectories was found to be in agreement with the two key experimental results provided by the time-resolved neutron interferometry experiments.

SIGNIFICANCE Voltage-gated cation channels are central to neurological signal transmission. How they change conformation in response to changes in the transmembrane voltage remains unresolved. Time-resolved neutron interferometry experiments have determined directly the dependence of the profile structure of a voltage-gated K^+ channel within single phospholipid bilayers and of the distribution of water within that structure on the transmembrane voltage. These two key results were compared with their counterparts predicted by three different computational approaches for modeling the activated, open and deactivated, closed states of three different voltage-gated K^+ channels in hydrated phospholipid bilayers. Only one was found to be in agreement with the two key results. Thus, these time-resolved neutron interferometry experiments provide a crucial test for the computational modeling approaches.

INTRODUCTION

Nav and Kv channels are voltage-gated ion channels (VGICs) selective for sodium or potassium, respectively, that are responsible for the generation and propagation of action potentials in neurological signal transmission (1). The mechanism of coupling conformational changes within the four voltage sensor domains (VSDs) in response to a change in the transmembrane voltage, either depolarizing or polarizing relative to the resting voltage, to opening or closing the channel within the pore domain (PD) remains unknown (2,3). The VSDs of VGICs are deactivated at the resting transmembrane voltage of −60 to −70 mV and experience the absence of a transmembrane voltage only

Submitted February 11, 2019, and accepted for publication July 9, 2019.
*Correspondence: jkblasie@sas.upenn.edu
Editor: Michael Grabe.
https://doi.org/10.1016/j.bpj.2019.07.011

transiently during the course of an action potential of a few milliseconds' duration (4). To date, higher-resolution three-dimensional (3-D) structures for VGICs have only been provided by conventional techniques (x-ray crystallography, cryo-electron microscopy) in the absence of a transmembrane voltage (e.g., 5–7). This seriously complicates any investigation into the mechanism of electromechanical coupling. For example, in the case of Kv channels for which the first high-resolution structures were obtained, the channel within the PD was found to be open, and the conformations of the VSDs were assumed to be activated because 0 mV would be sufficiently depolarizing (5,8). In the absence of a structure for the deactivated, closed state of Kv channels, numerous models were developed employing various computational approaches, each relying on specific assumptions (2,3). Several incorporated restraints based on experimental results provided by indirect techniques (9–13). For example, one utilized pairs of site-directed cysteine mutations and measurements of metal cross-linking as a function of the transmembrane voltage (14). Other approaches attempted to induce the deactivated, closed state by applying hyperpolarizing transmembrane voltages (e.g., 15–17). The most successful of these utilized very long 250 μs MD simulations (18). Overall, such studies demonstrated a high degree of similarity in the atomic models, thereby achieving a "consensus" structure for the deactivated, closed state of Kv channels (2). However, despite the "consensus" noted, experimental validation utilizing one or more direct techniques remains essential.

Some developments were needed to investigate the voltage-dependent structures of VGICs directly, without having to resort to one or more site-directed mutations and subsequent labeling with bulky chromophores or heavy metals. We first developed two methods for the fabrication of single-membrane specimens, composed of a phospholipid bilayer containing a vectorially oriented voltage-gated K^+ channel protein at high in-plane density, tethered to the surface of an inorganic multilayer substrate to allow for the application of transmembrane voltages in an electrochemical cell (19,20). The structures of the tethered single-membrane specimens were then characterized by both x-ray reflectivity (19) and neutron reflectivity (21), each enhanced by interferometry enabled by the multilayer substrate (20,22). The electrical properties of the membranes were characterized by electrical impedance spectroscopy (EIS). With these essential developments, we then utilized time-resolved x-ray and neutron interferometry to investigate the dependence of the so-called "profile structure" of the isolated VSD of the prokaryotic Kv channel KvAP on physiologically relevant transmembrane voltages that were nonpolarizing, polarizing, and depolarizing with respect to the transmembrane resting voltage (23). The profile structure is the projection of the 3-D structure of the membrane parallel to the membrane plane onto the membrane normal and is dominated by the protein component at the high in-plane density. In these time-resolved, "pump-probe" experiments, the three voltages were applied cyclically, and the interferometry data were collected separately for each voltage and subsequently averaged. For the x-ray case employing a pulsed synchrotron source, radiation damage to the specimens was detected after only three voltage cycles, although the incident photon flux was sufficiently high to provide accurate x-ray scattering-length density (xSLD) profiles for each voltage within a single cycle. For the neutron case utilizing a pulsed spallation source, the incident neutron flux was dramatically lower, therefore requiring many voltage cycles to provide accurate neutron scattering-length density (nSLD) profiles made possible by the absence of any detectable radiation damage to the specimens. The voltage-dependent xSLD and nSLD profile structures for the isolated VSD of KvAP determined from these time-resolved experiments were found to be in good agreement with long (multi-μs) molecular dynamics (MD) simulations of the same VSD protein within a hydrated phospholipid bilayer membrane investigated as a function of similar physiologically relevant transmembrane voltages (24).

In this work, we extended our time-resolved neutron interferometry approach to investigate the dependence of the profile structure of the complete homotetrameric prokaryotic Kv channel KvAP, vectorially oriented within a phospholipid bilayer membrane at a solid-liquid interface, on the transmembrane voltage. A cyclic sequence of hyperpolarizing and depolarizing voltage pulses, whose amplitudes and duration were judiciously selected to circumvent the inactivation exhibited by the complete homotetrameric channel (25), was synchronized with the pulsed neutron source. Averaging the data for each of the hyperpolarizing and depolarizing voltage pulses collected over many cycles provided the nSLD profile structure of the membrane for the deactivated, closed state (hyperpolarized) and activated, open state (depolarized) of the channel, as well as the profile structure for water within the Kv channel for these two end states, the latter enabled by using neutrons (20). There were two key experimental results from this study, namely the difference ΔnSLD profile structures for both the membrane and for water within the membrane, each calculated as the nSLD profile for the deactivated, closed state (hyperpolarized) minus the nSLD profile for the activated, open state (depolarized). The two key results were then compared with those predicted by three fundamentally different computational approaches to modeling these same two states for three different voltage-gated K^+ channels in hydrated phospholipid bilayer membranes. They included a targeted MD simulation applied to the prokaryotic KvAP channel (13), ROSETTA membrane protein structure prediction followed by MD simulation applied to the transmembrane domain of the eukaryotic Kv1.2 channel (9–11), and a state-of-the-art, 250 μs timescale MD simulation (18) applied to the transmembrane domain of the

eukaryotic Kv1.2/2.1 chimera channel. Only one of these computational approaches was found to be in agreement with both of the two key experimental results for the KvAP channel provided by our time-resolved neutron interferometry experiments.

MATERIALS AND METHODS

Expression and purification of KvAP protein

The KvAP gene (coding for residues 14–295 of the protein) was amplified from a PQE60 plasmid that was kindly provided by Dr. Rod McKinnon (Rockefeller University). The gene was inserted into the in-house pETCH vector (26), which supplies a C-terminal His_6 tag. The plasmid was inserted into C41(DE3) cells, which were grown in Luria-Bertani medium at 37°C. When the OD_{600} value reached 0.8, protein expression was induced by addition of 0.4 mM isopropylthiogalactoside; 10 mM $BaCl_2$ was added to the medium at the same time. Cells were harvested after 4 h, washed with water, and frozen.

All purification steps were carried out at 4°C. Cells were lysed in 20 mM Tris (pH 8), 100 mM KCl (buffer A) using an Emulsiflex cell disruptor (Avestin Inc., Ottawa, Ontario, Canada) operating at 20,000 psi. The lysate was centrifuged at 14,000 × *g* for 15 min, after which the supernatant was centrifuged at 200,000 × *g* for 1 h to isolate the membrane fraction. The membrane pellet was resuspended in buffer A, and *n*-decyl-*β*-D-maltopyranoside (DM) was added to a final concentration of 1.9% (w/v). After 1 h, the suspension was centrifuged again at 200,000 × *g* for 1 h. The supernatant was filtered and applied to a 1 mL HisTrap-HP column (GE LifeSciences, Pittsburgh, Pennsylvania) equilibrated with buffer A + 0.24% DM. KvAP was eluted with a gradient from 0 to 400 mM imidazole. Fractions containing KvAP were pooled and dialyzed versus buffer A + 0.24% DM. The protein was then reduced with 1 mM tris(2-carboxyethyl)phosphine for an hour, after which it was concentrated to ~10 mg/mL. DM concentrations in the concentrated protein sample were measured by analytical thin-layer chromatography (27) and were typically found to be ~5% (w/v). A sample of the concentrated protein was analyzed by size-exclusion chromatography on a Sephacryl S-200 column in buffer A + 0.24% DM and found to migrate as a tetramer. Aliquots of the concentrated protein were flash-frozen in liquid nitrogen.

Specimens for x-ray interferometry and time-resolved neutron interferometry experiments

We used a modified version of the self-assembly method (19) to tether the homotetrameric KvAP solubilized in DM, designated as KvAP-DM, to the surface of an Si-Ge-Si multilayer on silicon substrates to result in a unique vectorial orientation of the KvAP protein with respect to the normal to the substrate surface. The modifications included utilizing 3-aminopropyldimethylethoxysilane (Gelest, Morrisville, PA) to alkylate the silicon oxide surface of the substrate, followed by sequential reaction with three linkers—succinic anhydride (Sigma-Aldrich, St. Louis, MO), 1-ethyl-3(3-dimethylaminopropyl)carbodiimide hydrochloride (Pierce Biotechnology, Rockford, IL), and N-hydroxysuccinimide (Pierce)—followed by surface functionalization with $N_\alpha N_\alpha$-Bis(carboxymethyl)-L-lysine hydrate (Sigma-Aldrich) to produce an alkylated substrate surface possessing nitrilotriacetate endgroups. The modifications resulted in improved specimen-to-specimen reproducibility for tethering KvAP-DM to the surface of the Si-Ge-Si multilayer on silicon substrates. Each silicon or germanium layer in the multilayer was of ~20 Å thickness, fabricated by magnetron sputtering at the Advanced Photon Source, Argonne National Laboratory. The detergent was subsequently exchanged for 1-palmitoyl-2-oleoylphosphatidylcholine (POPC; Avanti Polar Lipids, Alabaster, AL) following the self-assembly method (19).

Electrochemical cell for time-resolved neutron interferometry experiments

The basic features of the electrochemical cells used for the time-resolved neutron interferometry experiments reported herein were similar to those for the cells used previously for the closely related experiments with the isolated VSD from KvAP (23). Here, instead of an Si-Ni-Si multilayer on silicon substrate as in the reference, the working electrode was provided by an Si-Ge-Si multilayer on a silicon substrate, the latter being heavily doped with phosphorus to make it sufficiently conductive ($R < 1\ \Omega cm^2$), which was held at ground potential. The electric potential (voltage) was applied to the membrane on the surface of the Si-Ge-Si multilayer substrate via a platinum counterelectrode in the aqueous electrolyte composed of 0.1 M KCl in 1 mM Tris buffer at pH 8. For either the isolated VSD studied previously (23) or KvAP itself tethered to the substrate surface via a His-tag on the protein's C-terminus in this study, this is exactly opposite to the electrophysiological convention in which the extracellular side of the membrane is at ground potential and the electric potential is applied to the cytoplasmic side.

Design of the neutron interferometry "pump-probe" experiment to avoid KvAP inactivation

In a classic "pump-probe" experiment, the membrane containing the vectorially oriented Kv channel is subjected to a periodic alternating sequence of polarizing and depolarizing pulses with respect to the resting transmembrane voltage, each of constant amplitude and finite duration, and the membrane structure is synchronously probed with a small number of neutron pulses for each voltage pulse applied to the membrane. This approach has the absolute requirement that both the activation of the four VSDs and subsequent opening of the channel within the PD produced by the depolarizing voltage pulse and the deactivation of the four VSDs and closing of the channel within the PD produced by the polarizing voltage pulse be completely reversible. Utilizing a pulsed neutron source like the Spallation Neutron Source at Oak Ridge National Laboratory, although the incident neutron pulses are of only ~10 μs duration, the momentum transfer $\bar{Q}$ (see Supporting Materials and Methods, Section a) for each scattered neutron is determined by time of flight (TOF), which requires 16.5 ms. Hence, the number of neutron pulses employed for each voltage pulse depends on the duration of the TOF, down to the lower limit of one neutron pulse for a voltage pulse of 16.5 ms duration.

However, all Nav and Kv channels exhibit inactivation, even those that do not possess the additional cytoplasmic domain of eukaryotic channels but only a transmembrane domain, like the prokaryotic Kv channel KvAP utilized in this work. For an ensemble of channels, only a fraction of the ensemble can be activated in response to a second, sufficiently depolarizing voltage pulse to result in pore opening and a measurable potassium current if the first depolarizing pulse is of too long a duration. For KvAP, using polarizing pulses of −120 mV and depolarizing pulses of +100 mV (electrophysiological convention), each of 150 ms duration, only about one third of the ensemble can be activated by a second depolarizing pulse (25). After four pulses, the entire ensemble is inactivated. Unfortunately, reactivation occurs only on a much longer timescale, namely ~90 s for KvAP incorporated into a planar phospholipid bilayer composed of POPC:1-palmitoyl-2-oleoylphosphatidylglycerol (POPG)-decane (25). This situation would render such a "pump-probe" experiment as described above essentially impossible because the experiment would be exceedingly inefficient, utilizing only an infinitesimal fraction (1/600) of the incident neutron flux available, noting the incident neutron pulse rate of 60 Hz, to achieve the requirement of complete reversibility. However, a judicious choice of both the amplitude and duration of the polarizing and depolarizing voltage pulses can be used to circumvent inactivation for a particular Kv channel depending on its membrane environment. As shown in Fig. 4 of (25), choosing more hyperpolarizing pulses

of −150 mV and less depolarizing pulses of +20 mV, each of only 50 ms duration, can be employed to eliminate any measurable inactivation for KvAP in a planar phospholipid bilayer composed of POPC:POPG-decane. As a result of the above considerations, we employed three neutron pulses for each hyperpolarizing or depolarizing voltage pulse, this number averaging over the complete activation of the KvAP channel ensemble upon application of each depolarizing voltage pulse from inspection of Fig. 1 of (25).

X-ray interferometry data collection

X-ray interferometry data were collected from several specimens, each composed of either a KvAP-DM monolayer or a KvAP-POPC membrane after POPC-DM exchange, tethered to the surface of the same Si-Ge-Si multilayer substrate. The specimens were maintained in a hydrated state with moist He at 95% relative humidity in a thermoregulated specimen chamber with Kapton windows. Specular x-ray reflectivity data were collected at 8.048 keV (1.543 Å), using a rotating-anode x-ray source, singly bent LiF monochromator incident beam optics, a Huber 4-circle diffractometer (Huber, Rimsting, Germany), an Si(111) analyzer, and a scintillation detector, via θ-2θ scans as described previously (19). These data were subsequently corrected for the incident beam footprint on the planar specimen depending on the angle of incidence and for off-specular background scattering.

Time-resolved neutron interferometry data collection

Time-resolved neutron interferometry data were collected with the Magnetism Reflectometer on Beamline 4A at the Spallation Neutron Source, Oak Ridge National Laboratory (28). Several specimens were investigated, composed of either a KvAP-POPC membrane tethered to the surface of an Si-Ge-Si multilayer substrate (four) or just the self-assembled monolayer (SAM) used to tether KvAP-DM to the substrate as a voltage-insensitive "control" (two). The incident neutron pulses are polychromatic and of ∼10 μs duration at a repetition rate of 60_Hz. 16.5 ms is required to determine the momentum transfer vector $\bar{Q}$ of each reflected neutron via TOF. The cyclic sequence of hyperpolarizing voltage pulses of 150 mV and depolarizing voltage pulses of 20 mV, each of 50 ms duration and constant amplitude, were synchronized with the incident neutron pulses so that there were three neutron pulses for each voltage pulse. To achieve acceptable reflected neutron counting statistics, reflectivity data were collected from each specimen for 3–200 min, for each of the six angles of incidence employed to span the range of Q_z accessed using the polychromatic neutron pulses. The time required increased with angle of incidence, and the reflected neutrons for each triplet of neutron pulses were collected separately and subsequently averaged over each of the hyperpolarizing or depolarizing voltage pulses. Given the incident neutron pulse rate, this implies that the reflectivity data for each transmembrane voltage were averaged over 10^3–10^6 cycles of the voltage pulse sequence. The time-averaged specular reflectivity data for each transmembrane voltage was then calculated, and the time-averaged data were subsequently corrected for the incident beam footprint on the planar specimen depending on the angle of incidence and for off-specular background scattering.

X-ray interferometry data analysis

The specular x-ray interferometry data for the KvAP-DM monolayer and KvAP-POPC membrane specimens were analyzed using a constrained refinement approach analogous to that described previously (19) to provide their respective xSLD profile. The formalism and its implementation are fully described in the Supporting Materials and Methods, Section a.

Time-resolved neutron interferometry data analysis

The time-averaged specular neutron interferometry data for either the hyperpolarizing or the depolarizing voltage pulses was analyzed, using a constrained refinement approach analogous to that first described previously for a tethered protein monolayer at the solid-gas interface (29), to provide the nSLD profile for each voltage. The formalism and its implementation are fully described in the Supporting Materials and Methods, Section a.

Estimation of error propagation in the x-ray and neutron interferometry data analysis

As described in the Supporting Materials and Methods, Section a, our data analysis employs the Fresnel-normalized x-ray or neutron interferometry data $R(Q_z)/R_F(Q_z)$, in which the specular reflectivity data $R(Q_z)$ containing the standard errors determined by the photon/neutron counting statistics has been divided by an analytic function $R_F(Q_z)$ describing the reflectivity from a single ideal interface. The constrained refinement approach employs Fourier transformations to produce the xSLD or nSLD profile structures that obscure the standard errors in the reflectivity data. For the x-ray case, the propagation of errors from the data into the xSLD profiles was estimated utilizing a region of the profile that should be of constant xSLD. As shown in Fig. 2 *A*, this occurs for the KvAP-DM specimens over the region 50 Å $< z <$ 100 Å, which is occupied by only the moist helium environment. The low-amplitude oscillations about zero xSLD in this region arise from error propagation with a wavelength determined by the truncation of the inverse Fourier transformation at a maximal Q_z of 0.427 Å^{-1}. For the neutron case, the time-resolved experiments employed "control" specimens composed of only the Si-Ge-Si multilayer substrate on silicon and the organic SAM, otherwise used to tether the KvAP-POPC membrane to the substrate's surface. These control specimens were not expected to exhibit any dependence on the transmembrane voltage applied to the KvAP-POPC membrane specimens. As shown in Fig. 4 *C*, the difference ΔnSLD profile for the SAM specimen (hyperpolarizing − depolarizing) over the region 0 Å $< z <$ 100 Å, otherwise occupied by the KvAP-POPC membrane when present, exhibits only low-amplitude oscillations about zero nSLD in this region. These low-amplitude oscillations arise from error propagation with a wavelength determined by the truncation of the inverse Fourier transformation at a maximal Q_z of 0.194 Å^{-1}. Because errors propagate in difference ΔnSLD profiles as the square root of the sum of the squares of the errors in each nSLD profile contributing to the difference profile, the standard errors in each contributing nSLD profile are then smaller by a factor of $1/\sqrt{2}$.

Modeling the voltage-dependent nSLD profiles for the KvAP-POPC membrane

We believe that it is essential that all-atom MD simulation be incorporated in any approach to modeling either the activated, open state or the deactivated, closed state of a Kv-channel protein within a hydrated phospholipid bilayer environment for two reasons. First, the elastic scattering experiment (neutron interferometry) is sensitive only to the time average over the dynamics inherent in such a membrane system. Second, upon embedding a particular state of the protein within the hydrated phospholipid bilayer, the protein must be allowed to relax in response to its environment within the bilayer, and conversely, the hydrated bilayer must be allowed to relax in response to the embedded protein. These processes cannot be accurately modeled using static structure representations. In Supporting Materials and Methods, Section c, we describe in detail the modeling of the activated, open and deactivated, closed states of three Kv channels in a hydrated phospholipid bilayer. These include the transmembrane domain of the eukaryotic Kv1.2/2.1 chimera, the transmembrane domain of the eukaryotic

Kv1.2, and the prokaryotic KvAP. Importantly, we also describe how the atomic-level detail in the MD simulations is utilized to produce the time-averaged nSLD profiles for either the entire membrane or the nSLD profiles for the separate protein, lipid, and water components for comparison with their experimental counterparts. A portion of the MD trajectories for either the activated, open state or the deactivated, closed state of Kv channel in the hydrated POPC bilayer was selected over which the system demonstrated stability. These portions were the same length for each state and were sampled at uniform intervals to generate a number of instantaneous configurations of the system used to calculate the time-averaged nSLD profiles. For the membrane, the atom selection included the protein, water, and lipid within a cylinder of defined radius that extended from the center of the protein outward perpendicular to the transmembrane axis. Each selected atom was binned into 0.5 Å steps along the transmembrane axis for each of the sampled configurations. The neutron atomic scattering lengths were summed for each bin, and these values were averaged over all sampled configurations to construct the time-averaged nSLD profile for each state of the Kv channel. The origin was defined as the protein center of mass for each configuration. Different deuteration ratios were achieved by randomly selecting a fraction of the hydrogen atoms on water and polar hydrogens on the protein to replace with deuterium. The same approach was employed to calculate the separate time-averaged nSLD profiles for the protein, lipid, and water components of the membrane as determined by the atom selection.

For the activated, open state of both the Kv1.2/2.1 chimera and the KvAP channel in a hydrated POPC bilayer membrane, we also calculated the resolution-limited nSLD profiles of the separate protein and lipid components. This was accomplished by the least-squares fitting of slab models (21), based on a finite sum of error functions, to the time-averaged nSLD profiles for either the activated, open state of the protein or the host POPC bilayer, each hydrated with 100% D_2O. Their resolution-limited counterparts were then calculated via Fourier transformation into momentum transfer space (Q_z), followed by inverse Fourier transformation back into real space (z) at somewhat higher spatial resolution than in the experimental nSLD profiles using twice the maximal value of Q_z (i.e., 2×0.194 Å^{-1}) in the time-resolved neutron interferometry experiments (see Supporting Materials and Methods, Section a). Thus, the minimal wavelength component in these resolution-limited nSLD profiles is half that of the experimental nSLD profiles, allowing important visualization of the influence of somewhat finer details in the model profiles on their overall shape at the experimental spatial resolution. Linear combinations of the separate resolution-limited nSLD profiles for the activated, open state of the protein and the host POPC bilayer hydrated with D_2O were then calculated, thereby allowing for manipulation of the lipid/protein mole ratio to match that of the experimental KvAP-POPC membrane employed in the time-resolved neutron interferometry experiments. This was essential for the Kv1.2/2.1 chimera protein because the MD simulation cell contained twice the amount of POPC compared with that for the experimental KvAP-POPC membrane.

Supporting material

The analysis of the x-ray interferometry data and the time-resolved neutron interferometry data is fully described in Supporting Materials and Methods, Section a, and specimen-to-specimen reproducibility with regard to the time-resolved neutron interferometry experiments is addressed in Supporting Materials and Methods, Section b. The details of the MD simulations for modeling the activated, open state and the deactivated, closed state of three Kv channels in a hydrated POPC bilayer membrane environment, including the Kv1.2/2.1 chimera, Kv1.2, and KvAP, are described in Supporting Materials and Methods, Section c. The effect of the experimental spatial resolution on our ability to detect smaller translations of the S4 helix within the VSDs of the Kv channels associated with the transition between the activated, open state and the deactivated, closed state is described in Supporting Materials and Methods, Section d.

RESULTS

Folding KvAP at the solid-liquid interface

Based on a comparison of the x-ray crystal structures for the prokaryotic KvAP channel determined in a detergent micellar environment (30) and the eukaryotic Kv1.2 channel determined in a mixed phospholipid-detergent micellar environment (8), it was proposed (31) that the VSDs of KvAP would undergo refolding to form a four-helix bundle motif and a substantial reorientation of the bundle axis upon transfer from a micellar detergent environment to that of a phospholipid bilayer. Thus, we first investigated the profile structure of KvAP-DM within a monolayer tethered to the surface of an Si-Ge-Si multilayer substrate and subsequently the profile structure of the tethered KvAP-POPC membrane after detergent-phospholipid exchange employing the self-assembly method, performing x-ray interferometry after each stage of fabrication in a moist helium environment (19). Numerous specimens were investigated using both Si-Ge-Si multilayer substrates (four) as well as monolayer graphene on Si-Ge-Si multilayer substrates (four). For the latter, tethering the KvAP-DM monolayer to the graphene surface was achieved as in (32). In Fig. 1, we show typical Fresnel-normalized specular x-ray reflectivity data for the specimens on Si-Ge-Si multilayer substrates. Fig. 1 *A* shows the data for the substrate possessing only the organic self-assembled monolayer (SAM) used subsequently to tether the KvAP-DM monolayer to its surface, Fig. 1 *B* for the substrate with the tethered KvAP-DM monolayer on its surface, and Fig. 1 *C* for the substrate with the tethered KvAP-POPC membrane on its surface after POPC-DM exchange. The error bars are based on the photon-counting statistics. In Fig. 2 *A*, we show the xSLD profile for a typical KvAP-DM monolayer on the surface of either an Si-Ge-Si multilayer substrate or a monolayer graphene on Si-Ge-Si multilayer substrate using the constrained refinement approach. The horizontal dotted lines above and below the abscissa were used to estimate the propagation of errors from the reflectivity data into the xSLD profiles, described in Estimation of Error Propagation in the X-Ray and Neutron Interferometry Data Analysis. For the tethered KvAP-DM monolayers on either substrate, the xSLD profile of the monolayer occurred relatively close to the substrate's surface. In Fig. 2 *B*, we show the xSLD profiles for the Si-Ge-Si multilayer substrate with the KvAP-DM monolayer on its surface compared with only the SAM on its surface. The best xSLD profile for the KvAP-DM monolayer itself is the difference of these two profiles as shown in Fig. 2 *C* with estimated propagated error bars as described. Also shown in Fig. 2 *C*, the xSLD profile for the KvAP-DM monolayer can be seen to agree fairly well with that calculated from the x-ray crystal structure from (30). All specimens for the tethered KvAP-DM monolayer exhibited similar xSLD profiles. As shown in Fig. 2 *D*, there

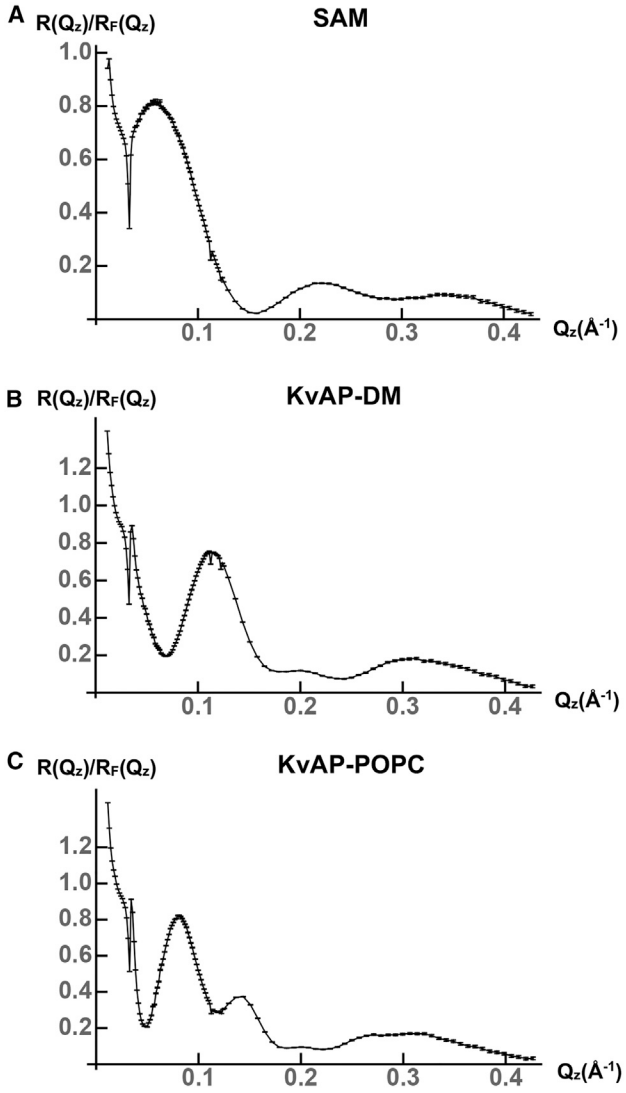

FIGURE 1 Fresnel-normalized x-ray interferometry data $R(Q_z)/R_F(Q_z)$ with regard to folding KvAP at the solid-liquid interface. (*A*) $R(Q_z)/R_F(Q_z)$ data for the organic self-assembled monolayer (SAM) used to tether the KvAP-DM monolayer to the surface of an Si-Ge-Si multilayer substrate are shown. (*B*) $R(Q_z)/R_F(Q_z)$ data for a KvAP-DM monolayer tethered to the surface of an Si-Ge-Si multilayer substrate are shown. (*C*) $R(Q_z)/R_F(Q_z)$ data for a KvAP-POPC membrane tethered to the surface of the same Si-Ge-Si multilayer substrate are shown. Error bars are based on the photon-counting statistics.

is a substantial change in the xSLD profile for the KvAP-POPC membrane after exchange of POPC for DM. The membrane is further from the substrate surface, and thus, subtraction of the xSLD profile of the substrate with the SAM on its surface is not required. The estimated propagated errors are the same as for the KvAP-DM monolayer, noting the small change in ordinate scale. In Fig. 2 *D*, we have also superimposed the xSLD profiles calculated for the model proposed in (31), as described in Fig. 2 *E*, as well as for rotations of the axis of the four-helix bundle VSDs of 5°, 10°, 15°, and 20° less than the 90° rotation originally proposed. As can be seen from Fig. 2 *D*, a rotation by only 10° less than the 90° rotation originally proposed brings the model into close agreement with the experimental xSLD profile for the KvAP-POPC membrane dominated by the KvAP protein. Based on the estimated propagated errors in the experimental xSLD profile, we estimate that the rotation has been determined with a precision of about $\pm 2°$. In Fig. 2 *F*, we compare the 3-D structure for KvAP originally proposed (31) with that found in our experiments.

A majority of the specimens exhibited xSLD profiles for the KvAP-POPC membrane as shown in Fig. 2 *D*, whereas a minority exhibited xSLD profiles intermediate between that for the precursor KvAP-DM monolayer and that for the KvAP-POPC membrane, suggesting incomplete exchange. EIS indicated a substantial increase in the resistance of the overlayer on the substrate's surface upon the transformation from the tethered KvAP-DM monolayer to a tethered KvAP-POPC membrane for all specimens. The resistance of the KvAP-POPC membrane tethered to the surface of graphene was 2.3×10^5–1.3×10^6 Ωcm^2, whereas that for the membrane tethered to the surface of silicon was 1.2×10^6– 4.7×10^6 Ωcm^2. Typical EIS data are shown in Fig. S1 for the SAM on a monolayer of graphene on an Si-Ge-Si multilayer substrate in Fig. S1 *A*, for the KvAP-POPC membrane on the same substrate in Fig. S1 *B*, and for a KvAP-POPC membrane on an Si-Ge-Si substrate in Fig. S1 *C*, along with the best model fits to the EIS data. The model utilized one R-RC circuit to represent the substrate and a second RC circuit in series to represent the bio-organic overlayer on its surface, either the SAM or the KvAP-POPC membrane. Thus, we concluded that a properly folded KvAP homotetramer within the POPC bilayer membrane, structurally homologous with Kv1.2 and capable of sensing changes in the transmembrane voltage, had been achieved.

Time-resolved "pump-probe" neutron interferometry

We utilized a cyclic sequence of hyperpolarizing voltage pulses of 150 mV and depolarizing voltage pulses of 20 mV, each of 50 ms duration, to circumvent inactivation of the KvAP channel ensemble within a POPC bilayer membrane. The sequence of voltage pulses and synchronized neutron pulse triplets is depicted in Fig. 3 *A*. The Fresnel-normalized neutron interferometry data $R(Q_z)/R_F(Q_z)$ for one KvAP-POPC membrane (specimen S2), averaged over either the hyperpolarizing or depolarizing voltage pulses with standard errors based on the neutron counting statistics, are shown for aqueous solvent contrasts of 60% D_2O/40% H_2O in Fig. 3 *B* and 90% D_2O/10% H_2O in Fig. 3 *C*. There are experimentally significant differences in the mean of the $R(Q_z)/R_F(Q_z)$ data that exceed the standard errors consistently over small ranges of momentum transfer Q_z for both contrasts, becoming more evident with increasing Q_z

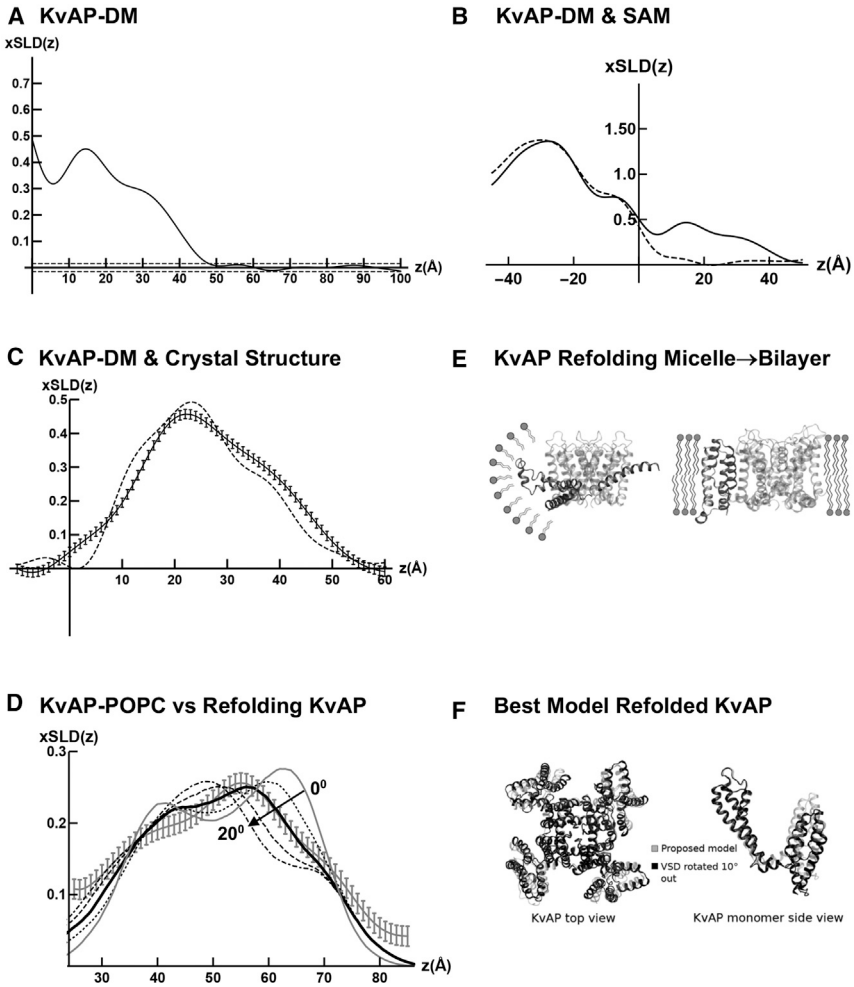

FIGURE 2 Folding KvAP at the solid-liquid interface. (*A*) The xSLD(z) profile for a KvAP-DM monolayer tethered to the surface of an Si-Ge-Si multilayer substrate is shown. The horizontal dashed lines above and below the abscissa were used to estimate the propagation of errors. (*B*) The xSLD(z) profiles for an Si-Ge-Si multilayer substrate with only the organic SAM used to tether the KvAP-DM monolayer to its surface (*dashed*) and for a slightly different Si-Ge-Si multilayer substrate with a KvAP-DM monolayer tethered to its surface (*solid*) are shown. The xSLD profiles for the multilayer substrates occur for $z < 0$ Å, whereas those for the SAM or tethered KvAP-DM monolayer occur for $z > 0$ Å. (*C*) The xSLD(z) profile for the tethered KvAP-DM monolayer (*solid*) with estimated errors is shown, compared with the xSLD(z) profile calculated from the x-ray crystal structure for KvAP-DM (*dashed*). (*D*) The xSLD(z) profile for the KvAP-POPC membrane after POPC-DM exchange (*gray* with estimated errors) is shown, compared with the xSLD(z) profiles calculated for the model proposed for KvAP (*gray solid*) within a phospholipid bilayer environment described in (*E*), as well as for rotations of 5° (*dotted*), 10° (*black solid*), 15° (*dashed*), and 20° (*dash-dot*) less than the 90° originally proposed. (*E*) An illustration is given showing the proposed (31) refolding of the S1 helix to form a four-helix bundle structure for the VSDs and reorientation of the bundle axis relative to the pore axis of KvAP via a rotation of ~90° upon the transformation from a detergent micelle environment (*left side*) to a phospholipid bilayer environment (*right side*). One VSD is shown in the foreground (*black*) with the PD in the background (*gray*). (*F*) Top view and side view (of one subunit) of the 3-D structure proposed for KvAP in a phospholipid bilayer environment from (31) is shown in a ribbon representation (*gray*), compared with that for a rotation of the VSDs by 10° less (*black*) than originally proposed. The xSLD(z) profiles are in units of electron density, $e^{-}/Å^{3}$.

and somewhat larger for 60% D_2O/40% H_2O. Four different KvAP-POPC membrane specimens were investigated, and specimen-to-specimen reproducibility is addressed in Supporting Materials and Methods, Section b.

The nSLD profiles for specimen S2 at the aqueous solvent contrasts provided by 90% D_2O/10% H_2O and 60% D_2O/40% H_2O, derived from the $R(Q_z)/R_F(Q_z)$ data using the constrained refinement approach, are shown in Fig. 4. The nSLD profile for the Si-Ge-Si multilayer substrate occurs for $z < 0$ Å (data not shown), whereas the nSLD profile for the KvAP-POPC membrane occurs within the interval 30 Å $< z <$ 110 Å with the membrane centroid located at $z \sim 75$ Å. The nSLD profiles for the membrane appear at negative contrast with respect to the average nSLD of both electrolytes shown in Fig. 4 *A* (*left side*) for 90% D_2O and in Fig. 4 *B* (*left side*) for 60% D_2O. The changes in the membrane nSLD profiles for the hyperpolarizing versus the depolarizing voltage pulses occur within the interval 65 ± 35 Å for both contrasts. In general, they demonstrate a loss of nSLD within the extracellular half of the membrane for $z > 75$ Å and a gain of nSLD within the cytoplasmic half of the membrane for $z < 75$ Å, that exceed the estimated propagated errors, for the deactivated, closed state of the channel (hyperpolarized) relative to the activated, open state (depolarized). The difference ΔnSLD profiles, hyperpolarized minus depolarized, were calculated after superposition of the centroids of the nSLD profiles for the membrane at the maximal contrast provided by 90% D_2O for each transmembrane voltage. This was done so that the small shift in the centroid of the membrane nSLD profile for the hyperpolarizing voltage toward the substrate surface of less than 1 Å relative to that for the depolarizing voltage did not otherwise contribute to the difference ΔnSLD profiles. With this minor adjustment, the difference ΔnSLD profiles manifest the changes noted, as shown in Fig. 4 *A* (*right side*) for 90% D_2O and in Fig. 4 *B* (*right side*) for 60% D_2O, and although the changes are similar for both contrasts, they are larger for 60% D_2O. The difference

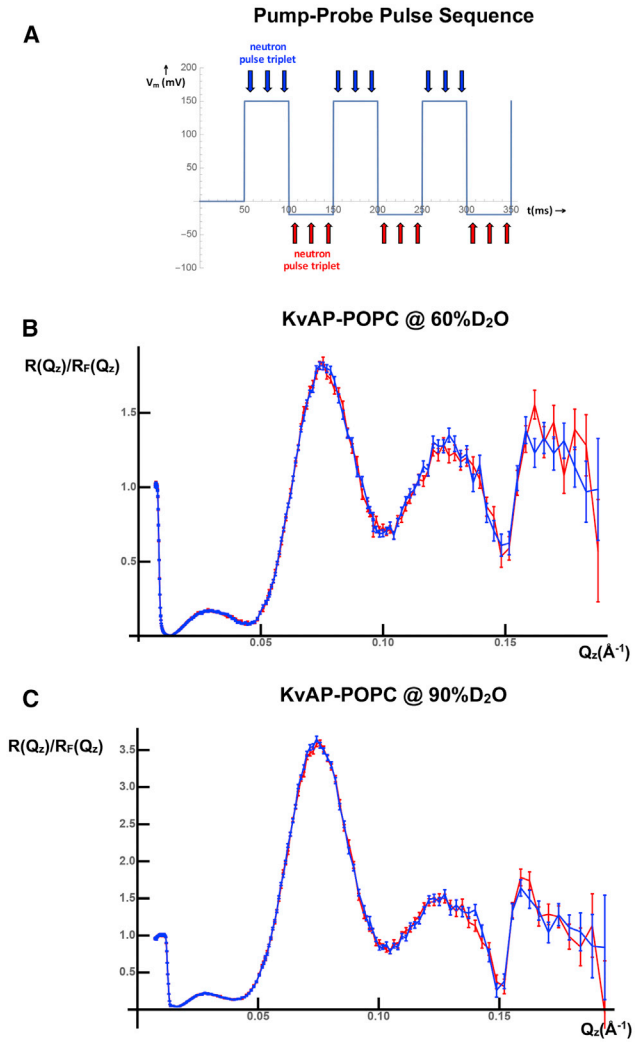

FIGURE 3 Time-resolved "pump-probe" neutron interferometry. (*A*) The cyclic sequence of hyperpolarizing and depolarizing transmembrane voltage pulses, together with the triplet of incident neutron pulses utilized for each voltage (*blue* hyperpolarizing, *red* depolarizing), employed in the time-resolved neutron interferometry experiment is shown. (*B*) Fresnel-normalized neutron reflectivity $R(Q_z)/R_F(Q_z)$, averaged over the hyperpolarizing voltage pulses (*blue*), is shown compared with that averaged over the depolarizing voltage pulses (*red*) for the KvAP-POPC membrane of specimen S2 at an aqueous solvent contrast of 60% D_2O/40% H_2O. (*C*) Similar Fresnel-normalized neutron reflectivity $R(Q_z)/R_F(Q_z)$ is shown for the same specimen at a contrast of 90% D_2O/10% H_2O. The standard errors for each are based on the reflected neutron counting statistics.

ΔnSLD profile for the control specimen S1 lacking the KvAP-POPC membrane is nearly featureless on the same ordinate scale as shown in Fig. 4 *C*. The horizontal dashed lines above and below the abscissa in Fig. 4 *C* were used to estimate the propagation of errors from the reflectivity data into the ΔnSLD profiles and the nSLD profiles described in Estimation of Error Propagation in the X-Ray and Neutron Interferometry Data Analysis. The different magnitudes of the features in the ΔnSLD profiles for the different contrasts arise from H-D exchange for both water and protein within the membrane profile because POPC possesses no exchangeable hydrogens.

The double-difference profile, $\Delta\Delta$nSLD, shown in Fig. 5 for 90% D_2O minus 60% D_2O and hyperpolarizing minus depolarizing voltages, provides the dependence of the H-D exchange profile on the transmembrane voltage. However, any water-accessible sites within the KvAP protein that might be unexposed for one state (e.g., deactivated, closed) and become exposed for the other state (e.g., activated, open) would all undergo H-D exchange because of cycling between the hyperpolarizing and depolarizing voltages. Hence, the double-difference profile, $\Delta\Delta$nSLD, in Fig. 5 is that for only water. The double-difference profile demonstrates that water is lost from the cytoplasmic half of the membrane for $z < 75$ Å, especially at the surface of the cytoplasmic side of the membrane at $z \sim$35–45 Å, and water is gained within the extracellular half of the membrane for $z \sim$85–95 Å, for the deactivated, closed state of the channel (hyperpolarized) relative to the activated, open state (depolarized). In Fig. 5, the nSLD profiles at 90% D_2O (hyperpolarized and depolarized) are shown in Fig. 5 *A* juxtaposed above the double-difference profile $\Delta\Delta$nSLD in Fig. 5 *B* for reference. The error bars in the double-difference profile $\Delta\Delta$nSLD are $\sqrt{2}$ larger than those in the ΔnSLD profiles, contributing to the difference described in Estimation of Error Propagation in the X-Ray and Neutron Interferometry Data Analysis.

Note that any model for the deactivated, closed state of the Kv channel relative to the activated, open state of the channel should predict both the ΔnSLD difference profiles and the $\Delta\Delta$nSLD double-difference profile from these time-resolved neutron interferometry experiments. This is because the experiments are directly sensitive to the voltage dependence of the profile structure of the Kv channel and to the voltage dependence of water within that profile structure in these single phospholipid bilayer membranes containing the vectorially oriented channel at high in-plane density. We compare several models for these two states of Kv channels in the sections that follow.

Modeling the nSLD profile for the activated, open state of the KvAP protein within a hydrated POPC bilayer membrane

We first address whether the nSLD profile structure determined for the KvAP-POPC membrane using a depolarizing transmembrane voltage to produce the activated, open state of the channel in our time-resolved neutron interferometry experiments is consistent with what is known about both the high-resolution structure of this Kv channel and the structure of a hydrated POPC bilayer. However, there is no x-ray crystal structure for a properly folded KvAP protein in the activated, open state. Instead, there is a model (31) based on a proposed structural homology for KvAP

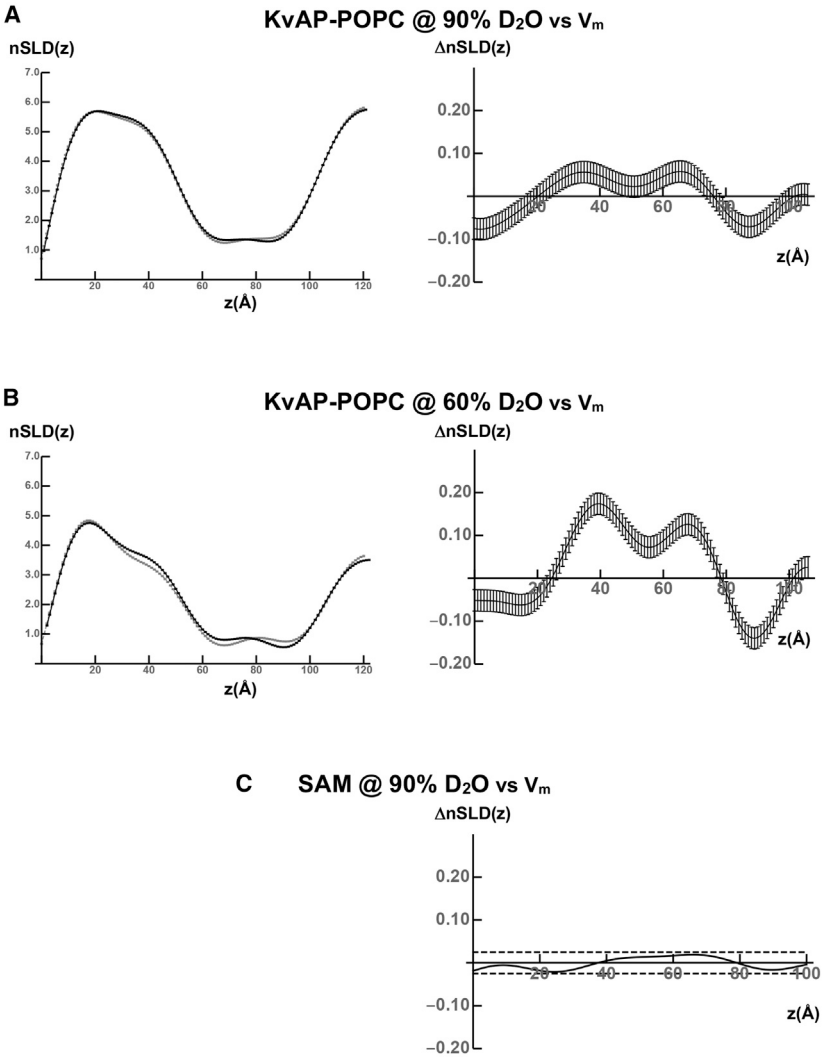

FIGURE 4 Experimental voltage-dependent profile structures for the KvAP-POPC membrane. (*A*) Left side shows the nSLD(z) profiles for the KvAP-POPC membrane of specimen S2 (*black* hyperpolarized, *gray* depolarized) at a solvent contrast of 90% D_2O/10% H_2O. The profile for the membrane is at negative contrast relative to 90% D_2O. (*A*) Right side shows the difference ΔnSLD(z) profile (hyperpolarized minus depolarized) at the same contrast of 90% D_2O/10% H_2O. (*B*) Left side shows the nSLD(z) profiles for the same specimen S2 at a contrast of 60% D_2O/40% H_2O. The profile for the membrane is also at negative contrast relative to 60% D_2O. (*B*) Right side shows the difference ΔnSLD(z) profile (hyperpolarized minus depolarized) at the same contrast of 60% D_2O/40% H_2O. (*C*) Right side shows the ΔnSLD(z) profile (hyperpolarized minus depolarized) for the organic SAM on the inorganic Si-Ge-Si multilayer substrate's surface, but otherwise lacking the tethered KvAP-POPC membrane, for specimen S1 at a solvent contrast of 90% D_2O/10% H_2O. The horizontal dashed lines above and below the abscissa were used to estimate the propagation of errors into the difference ΔnSLD(z) profiles and hence the nSLD(z) profiles contributing to the difference. The nSLD(z) profiles are in units of $10^{-6}/Å^2$.

with the transmembrane domain of Kv1.2 determined by x-ray crystallography (8) employing a more "membrane-like" crystallization environment, as described in Folding KvAP at the Solid-Liquid Interface. In Supporting Materials and Methods, Section c, we describe the construction of an improved model for this state of KvAP based on the result that the isolated VSD of KvAP was shown to undergo a substantial conformational change for depolarizing transmembrane voltages compared with the absence of a voltage (23,24). There are high-resolution x-ray crystal structures for the eukaryotic Kv channels, Kv1.2 (8) and the Kv1.2/2.1 chimera (5), with the highest resolution achieved for the latter. Given the proposed structural homology noted above, we first compare the time-averaged nSLD profile for the transmembrane domain of the Kv1.2/2.1 chimera protein in a hydrated POPC bilayer under a depolarizing transmembrane voltage from the MD simulation of (18), as described in Supporting Materials and Methods, Section c. We then compare the time-averaged nSLD profile for the improved model for KvAP in a hydrated POPC bilayer environment under a depolarizing transmembrane voltage in a MD simulation also described in Supporting Materials and Methods, Section c.

In Fig. 6 *A*, the left-side panel compares the time-averaged, resolution-limited nSLD profile of the activated, open state for the Kv1.2/2.1 chimera, based on the MD simulation within a hydrated POPC bilayer, with the experimental nSLD profile for the KvAP-POPC membrane at a depolarizing transmembrane voltage. The nSLD profile for the Kv1.2/2.1 chimera within a hydrated POPC bilayer was adjusted to match the lipid/protein mole ratio of the experiment. The right-side panel shows the separate resolution-limited nSLD profiles for both the Kv1.2/2.1 chimera protein and the POPC bilayer in D_2O, as well as their sum. In Fig. 6 *B*, the left-side panel compares the time-averaged, resolution-limited nSLD profile for the activated, open state of the KvAP protein, based on the MD simulation of the improved model within a hydrated POPC bilayer, with the experimental nSLD profile for the KvAP-POPC membrane at a depolarizing transmembrane voltage. The

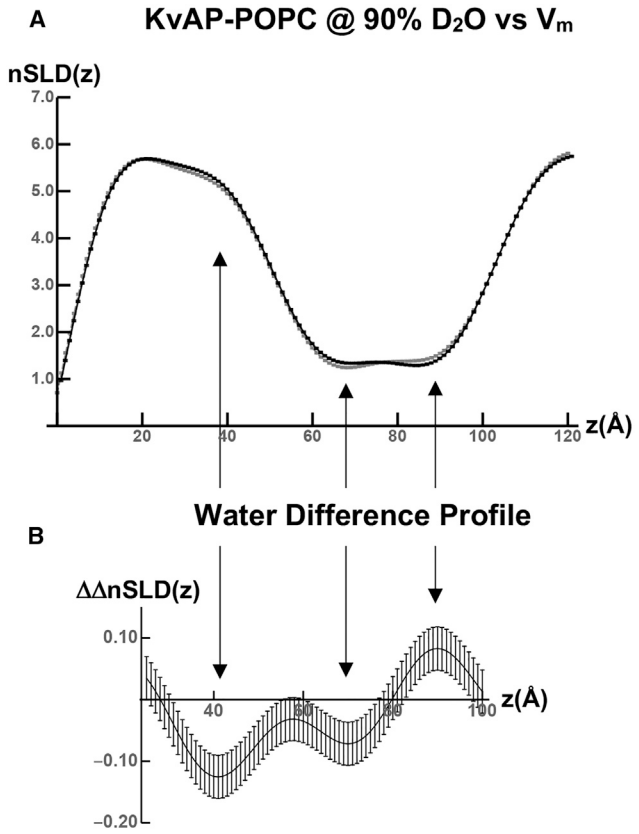

FIGURE 5 Experimental voltage-dependent profile structure for water within the KvAP-POPC membrane. (*A*) For reference, the nSLD(z) profiles for specimen S2 and an aqueous solvent contrast of 90% D_2O/10% H_2O from Fig. 4 are shown juxtaposed to better delineate those more relevant regions of the membrane profile exhibiting changes in the ΔnSLD(z) profile for water only (*vertical arrows*). (*B*) The double-difference $\Delta\Delta$nSLD(z) profile for solvent contrasts of 90% D_2O/10% H_2O minus 60% D_2O/40% H_2O and for hyperpolarizing minus depolarizing transmembrane voltages is shown for specimen S2. The estimated errors in the double-difference $\Delta\Delta$nSLD(z) profile are $\sqrt{2}$ larger than for the ΔnSLD(z) profiles shown in Fig. 4.

right-side panel shows the separate resolution-limited nSLD profiles for both the KvAP protein and the POPC bilayer in D_2O, as well as their sum.

In Fig. 6 *B*, the time-averaged, resolution-limited nSLD profile for the activated, open state of the KvAP protein within a hydrated POPC bilayer appears to be in reasonable agreement with the "double-well" geometric shape of the experimental nSLD profile for the KvAP-POPC membrane at a depolarizing transmembrane voltage. In Fig. 6 *A*, there is slightly less agreement between the time-averaged, resolution-limited nSLD profile for the activated, open state of the Kv1.2/2.1 chimera protein within a hydrated POPC bilayer and the "double-well" geometric shape of the experimental nSLD profile for the KvAP-POPC membrane at a depolarizing transmembrane voltage. This is not surprising based on the structural homology between the two proteins. For both the Kv1.2/2.1 chimera in Fig. 6 *A* and KvAP in Fig. 6 *B*, the more detailed features provided by the somewhat higher spatial resolution of the nSLD profiles for the models predict that the deeper minimum of the "double-well" geometric shape occurs within the cytoplasmic half of the membrane, as exhibited by the experimental nSLD profile, but to a lesser extent. Note that the separate nSLD profiles for the host POPC bilayer component are very similar, whereas the nSLD profiles for the protein component are more different, as shown in the right-side panels. Thus, any differences in the nSLD profiles for their respective membranes arise from the protein component. Lastly, if the spatial resolution in the resolution-limited nSLD profiles is reduced to approach that of the experimental profiles, the "double-well" geometric shape exhibited by the experimental profile is reproduced.

Modeling the difference ΔnSLD profiles between the deactivated, closed state and activated, open state of the KvAP protein within a hydrated POPC bilayer membrane

We next address whether any of the three fundamentally different computational approaches to modeling the deactivated, closed state and the activated, open state of a Kv channel mentioned in the Introduction can predict the experimental difference ΔnSLD profiles for the KvAP protein within a hydrated POPC bilayer membrane. Like for the experimental KvAP-POPC membrane, the difference ΔnSLD profiles described below were all calculated as the nSLD profile for the deactivated, closed state minus that for the activated, open state, after the superposition of the membrane centroids for each state of the respective Kv channel. Furthermore, the difference ΔnSLD profiles for each of the three models were calculated from their respective MD simulations described in Supporting Materials and Methods, Section c and smoothed via convolution with a Gaussian function ($\sigma = 5$ Å).

In Fig. 7 *A*, we show the difference ΔnSLD profile from the experiment for the KvAP-POPC membrane, with respect to the $z = 0$ Å origin at the substrate surface, for an aqueous solvent contrast of 60% D_2O. We chose the higher contrast for this comparison because the signal/noise level is higher than for 90% D_2O, and the following difference ΔnSLD profiles for the models are shown at the same contrast (60% D_2O). In Fig. 7, *B–D*, we show the difference ΔnSLD profiles for only the Kv1.2/2.1 chimera protein, for only the Kv1.2 protein, and for only the KvAP protein, respectively. In all of the ΔnSLD profiles for only the Kv-channel proteins, the $z = 0$ Å origin is at the membrane centroid.

There are three main features evident in the experimental difference ΔnSLD profile for the KvAP-POPC membrane shown in Fig. 7 *A*, namely the two maxima (max1, max2) and the minimum (min1) spanning ~70 Å of the membrane profile. These three features are very similar to those

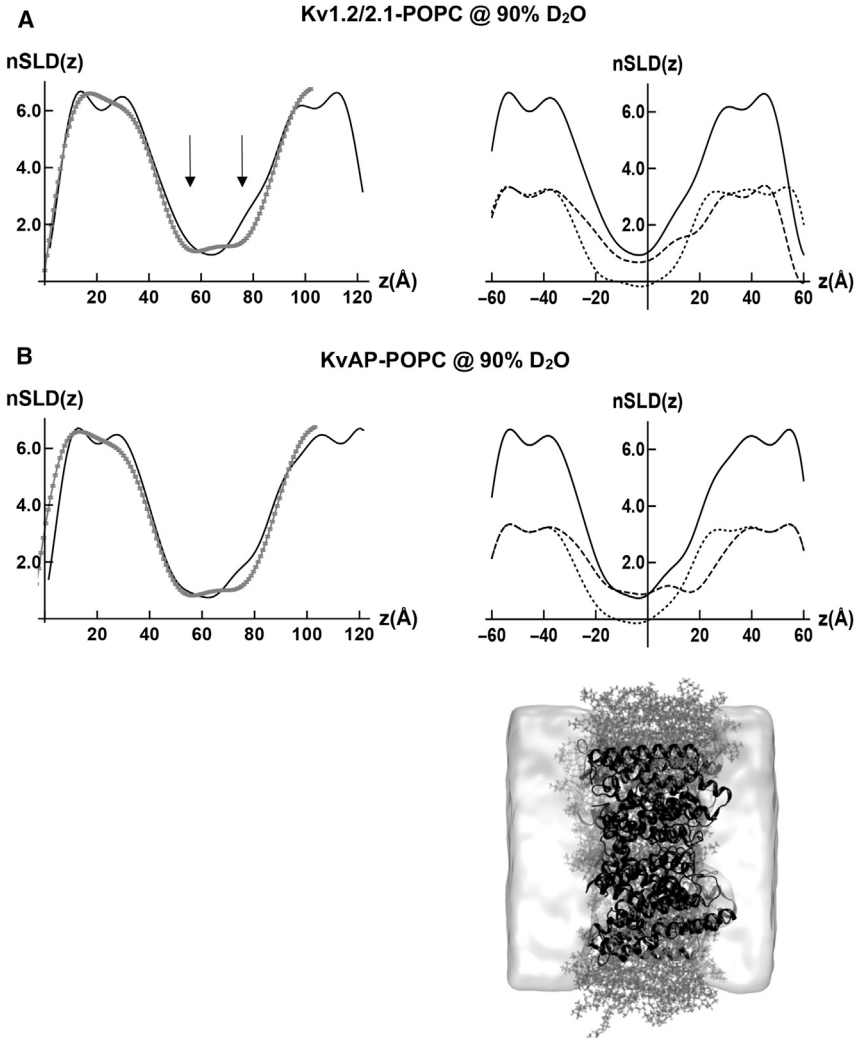

FIGURE 6 Modeling the nSLD profile for the activated, open state of KvAP in a hydrated POPC bilayer membrane. The nSLD profiles for the membranes in (*A*) and (*B*) below are at negative contrast relative to 90–100% D_2O. (*A*) Left side shows the experimental nSLD(*z*) profile for the KvAP-POPC membrane at a contrast of 90% D_2O/10% H_2O (*gray*) compared with that of the resolution-limited model based on MD simulation for the Kv1.2/2.1 chimera channel within a hydrated, POPC bilayer at a contrast of 100% D_2O (*black*) at twice the spatial resolution of the experimental profile. The two arrows point out the "double-well" shape of the experimental nSLD(*z*) profile. (*A*) Right side shows the separate contributions of the Kv1.2/2.1 protein (*dashed*) and the POPC bilayer (*dotted*) in 100% D_2O to the model profile and their sum (*solid*). (*B*) Left side shows the experimental nSLD(*z*) profile for the KvAP-POPC membrane at a contrast of 90% D_2O/10% H_2O (*gray*) compared with that of the resolution-limited model based on MD simulation of an improved model for this state of the KvAP channel within a hydrated, POPC bilayer at a contrast of 100% D_2O (*black*) at twice the spatial resolution of the experimental profile. (*B*) Right side shows the separate contributions of the KvAP protein (*dashed*) and the POPC bilayer (*dotted*) in 100% D_2O to the model profile, and their sum (*solid*). Juxtaposed below, we show to scale a rendering of an instantaneous configuration of the KvAP protein (*black ribbon*) embedded with the POPC bilayer (*gray licorice*) in a water slab (*white shaded*) from the MD simulation of the improved model for this state of the KvAP channel.

exhibited by the Kv1.2/2.1 chimera protein in Fig. 7 *B* and the Kv1.2 protein in Fig. 7 *C*, each spanning ~70 Å of their simulated membrane profile. The only exception is that the minimum between the two maxima within the cytoplasmic half of the membrane for the Kv1.2/2.1 and Kv1.2 proteins is much deeper than for the experimental KvAP-POPC membrane. This difference vanishes when the ΔnSLD profiles for the Kv1.2/2.1 and Kv1.2 proteins are convoluted with a broader Gaussian (e.g., σ ~10 Å) that matches the spatial resolution of the experimental ΔnSLD profile for the KvAP-POPC membrane. The similarity noted comparing the difference ΔnSLD profiles for only the protein components of the simulated membranes for Kv1.2/2.1 and Kv1.2 suggests that the experimental difference ΔnSLD profile for the KvAP-POPC membrane is dominated by its protein component. However, despite utilizing an improved model for the activated, open state of the KvAP protein, the major features in the difference ΔnSLD profile for only the protein in Fig. 7 *D* differ substantially from those for the experimental KvAP-POPC membrane in Fig. 7 *A*, especially within the extracellular half of the membrane.

With respect to the three main features in the experimental difference ΔnSLD profile in Fig. 7 *A*, the larger maximum occurs near the cytoplasmic surface of the membrane separated from a second maximum within the cytoplasmic half of the membrane by 28 Å, whereas the minimum occurs within the extracellular half of the membrane separated from the first maximum by 50 Å. The two separations of these three main features are the only unique attributes of the experimental ΔnSLD profile. It is notable that the ΔnSLD profiles for both the simulated Kv1.2/2.1 chimera protein and the simulated Kv1.2 protein within their respective POPC bilayer membranes exhibit the same three features, namely two maxima and one minimum that span their respective membrane profiles. As can be seen in Table 1, in which the separations noted utilize the centroids of the features, the two unique separations for the ΔnSLD profile of the Kv1.2/2.1 chimera protein match those of the KvAP protein to within less than 1 Å. However,

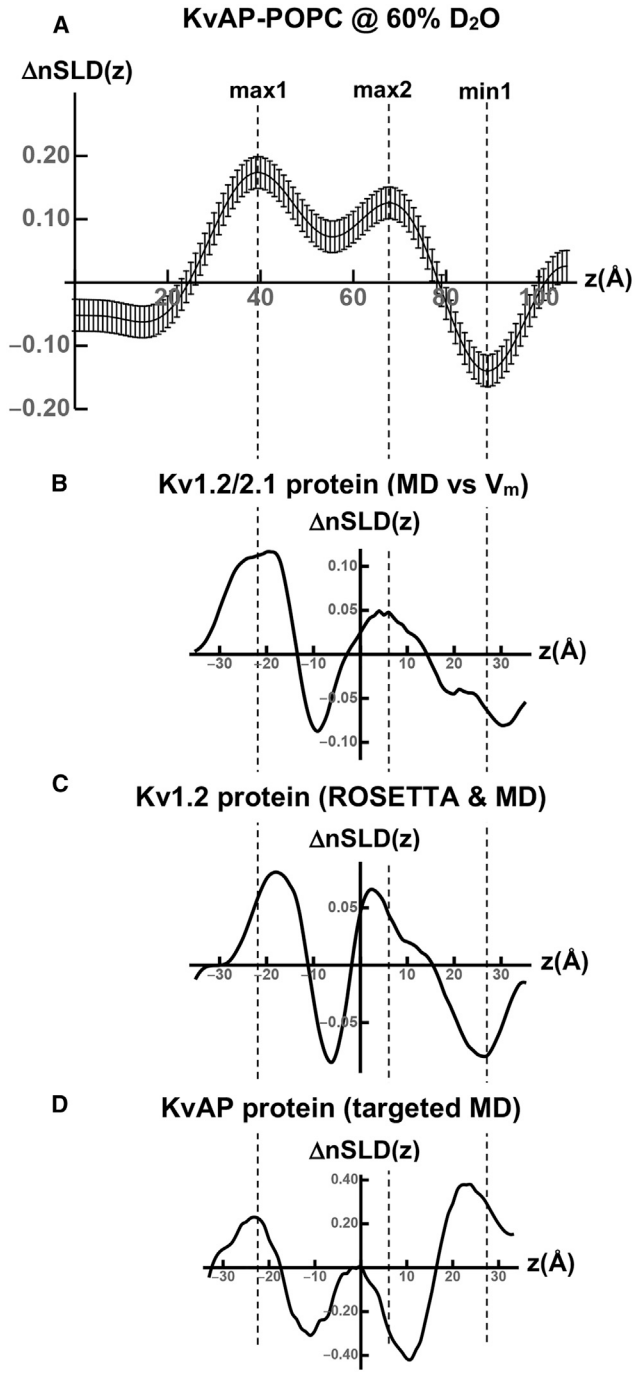

FIGURE 7 Modeling the difference ΔnSLD profile between the deactivated, closed and activated, open states of KvAP in a hydrated POPC bilayer membrane. (*A*) The experimental difference ΔnSLD(z) profile (hyperpolarized − depolarized) for the KvAP-POPC membrane is shown at a contrast of 60% D_2O/40% H_2O from Fig. 4 *B* with respect to the $z = 0$ Å origin at the multilayer substrate surface. (*B*) The difference ΔnSLD(z) profile (hyperpolarized − depolarized) for the Kv1.2/2.1 protein within a hydrated POPC bilayer membrane is shown at a contrast of 60% D_2O/40% H_2O with respect to the centroid of the membrane. The difference ΔnSLD(z) profile was calculated from MD simulations that utilized transmembrane voltages (V_m) to generate the deactivated, closed and activated, open states. (*C*) The difference ΔnSLD(z) profile for the Kv1.2 protein within a hydrated POPC bilayer membrane is shown at a contrast of 60% D_2O/40% H_2O with respect to the centroid of the membrane. The difference ΔnSLD(z) profile was calculated from MD simulations of ROSETTA models for the deactivated, closed and activated, open states. (*D*) The difference ΔnSLD(z) profile for the KvAP protein within a hydrated POPC bilayer membrane is shown at a contrast of 60% D_2O/40% H_2O with respect to the centroid of the membrane. The difference ΔnSLD(z) profile was calculated from targeted MD simulations to generate the deactivated, closed and activated, open states. The vertical dashed lines serve only to guide the eye.

the two unique separations for the ΔnSLD profile of the Kv1.2 protein are 6–8 Å smaller than for the KvAP protein. Thus, the question arises as to whether our time-resolved neutron interferometry experiments could have detected these smaller separations given the relatively low spatial resolution of the experimental nSLD profiles for the KvAP-POPC membrane at hyperpolarizing and depolarizing transmembrane voltages. The answer is "yes," as is demonstrated in Supporting Materials and Methods, Section d.

Modeling the difference ΔnSLD profile for water between the deactivated, closed state and activated, open state of the KvAP protein within a hydrated POPC bilayer membrane

Lastly, we address whether any of the three fundamentally different computational approaches to modeling the deactivated, closed state and the activated, open state of a Kv channel mentioned in the Introduction can predict the experimental difference ΔnSLD profile for water within the KvAP protein in a hydrated POPC bilayer membrane. As for the experimental KvAP-POPC membrane, the difference ΔnSLD profiles for water described below were calculated as the nSLD profile water for the deactivated, closed state minus that for the activated, open state after the superposition of the membrane centroids for each state of the respective Kv channel. Furthermore, the difference ΔnSLD profiles for water in each of the three models were calculated from their respective MD simulations described in Supporting Materials and Methods, Section c and smoothed via convolution with a Gaussian function ($\sigma = 5$ Å).

In Fig. 8 *A*, we show the experimental difference ΔnSLD profile for water within the KvAP-POPC membrane, namely the double-difference $\Delta\Delta$nSLD profile from Fig. 5 *B*. In Fig. 8 *B*, we show the difference ΔnSLD profile for water within the transmembrane domain of the Kv1.2/2.1 protein within a hydrated POPC bilayer. The agreement between the experimental and simulated difference nSLD profiles for water is seen to be very good, particularly with regard to both the amplitudes and signs of their major features, corresponding to the loss of water from the cytoplasmic half of the membrane, nearer the membrane surface, and the gain of water within the extracellular half of the membrane, nearer the membrane surface. They differ somewhat within the interior region of the membrane profile structure in between the two membrane surfaces, with some

TABLE 1 Separations between Features in the ΔnSLD Profiles

	Exp ΔnSLD KvAP	ΔnSLD Kv1.2/2.1	ΔnSLD Kv1.2
$\lvert\Delta(\text{max1} - \text{max2})\rvert$	28 Å	28 Å	20 Å
$\lvert\Delta(\text{max1} - \text{min1})\rvert$	50 Å	51 Å	44 Å

water being lost from the interior region for KvAP versus essentially none for the transmembrane domain of the Kv1.2/2.1 chimera. In Fig. 8 *C*, we show the difference ΔnSLD profile for water within the Kv1.2-POPC membrane. In this case, the difference ΔnSLD profile for water within the Kv1.2-POPC membrane bears no resemblance to that for the experimental KvAP-POPC membrane in terms of both amplitudes and signs of their respective features.

DISCUSSION

We chose to focus this investigation on the activated, open state and the deactivated, closed state of the prokaryotic KvAP channel, the endpoints of the electromechanical coupling mechanism in which all four VSDs of each channel in the ensemble are in the same fully activated or fully deactivated state. Intermediate states are also thought to play a role in the mechanism (3). Such intermediates can arise when some fraction of the four VSDs within each channel of the ensemble are either activated or deactivated. They can also arise when the VSDs are only partially activated or deactivated, with the translation of the S4 helices within the VSDs at some fraction of the maximal translation between the endpoints, e.g., 1/4, 1/2, or 3/4. We sought to avoid such intermediate states by utilizing depolarizing and hyperpolarizing transmembrane voltages whose amplitudes and duration were not only sufficient to circumvent inactivation but also sufficient to attain either full activation or deactivation of all four VSDs within each channel of the ensemble. The agreement achieved, as described in the next paragraph, suggests that we were successful.

The ΔnSLD profile for the Kv1.2/2.1 chimera protein from the MD simulations of (18) contains the effects of both a relatively large inward translation of the S4 helix within the VSDs of ~15 Å along the membrane profile, toward the cytoplasmic side of the membrane, and the closing of the channel of the PD in response to the hyperpolarizing transmembrane voltage. We found that the large inward translation of the S4 helix within the VSDs actually dominates the ΔnSLD profile over almost its full extent for the Kv1.2/2.1 protein except for the extreme cytoplasmic side of the profile, where changes in the PD near the C-terminus of the S6 helices also make a contribution, as shown in Fig. S3. In these simulations, the hyperpolarizing voltage was much larger than in our experiments, which could have contributed to the magnitude of this translation of the S4 helices (2). The agreement in terms of both the amplitudes and positions of the major features within the experimental ΔnSLD profile for the KvAP-POPC membrane and those in the ΔnSLD profile for the Kv1.2/2.1 chimera protein itself from the MD simulation is seen to

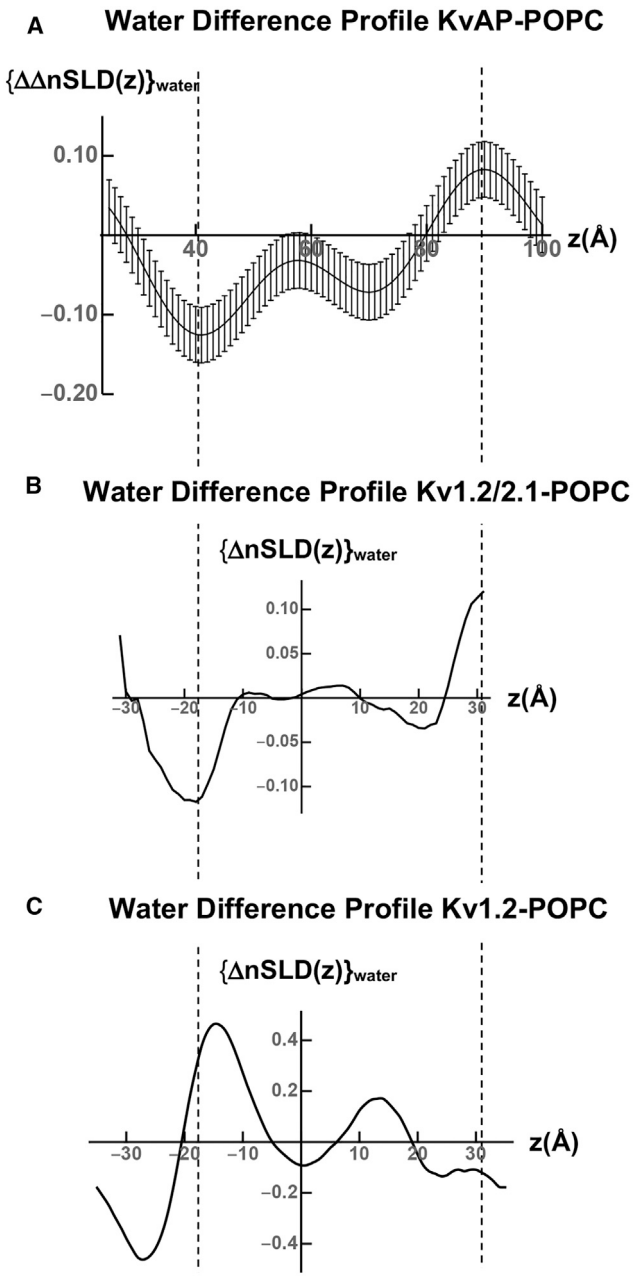

FIGURE 8 Modeling the difference ΔnSLD profile for water between the deactivated, closed and activated, open states of KvAP within a hydrated POPC bilayer membrane. (*A*) Experimental double-difference $\Delta\Delta$nSLD(z) profile for water within the experimental KvAP-POPC membrane from Fig. 5 *B* is shown. (*B*) The difference ΔnSLD(z) profile for water within the simulated Kv1.2/2.1-POPC membrane shown here with respect to the centroid of the nSLD profile for the membrane is shown. (*C*) The difference ΔnSLD(z) profile for water within the simulated Kv1.2-POPC membrane shown here with respect to the centroid of the nSLD profile is shown. The vertical dashed lines serve only to guide the eye.

be very good in Fig. 7, as quantified in Table 1. Although the major features in the difference ΔnSLD profile for the Kv1.2 protein in Fig. 7 *C* are qualitatively similar to those for both the Kv1.2/2.1 chimera protein in Fig. 7 *B* and for KvAP within the KvAP-POPC membrane in Fig. 7 *A*, the separations between the three features are 6–8 Å less for the Kv1.2 protein, using the vertical dashed lines as guides in Fig. 7 and as quantified in Table 1. It is noteworthy in this regard that the ΔnSLD profile from the simulation for the Kv1.2 protein contains the effects of both a smaller inward translation of the S4 helix within the VSDs of ∼7 Å along the membrane profile, toward the cytoplasmic side of the membrane, and the closing of the channel within the PD (10). As for the Kv1.2/2.1 protein chimera, we found that the smaller inward translation of the S4 helix within the VSDs also dominates the ΔnSLD profile over almost its full extent for the Kv1.2 protein. The differences in the separations of the main features in the difference ΔnSLD profiles for the Kv1.2/2.1 chimera protein versus the Kv1.2 protein noted above indicate the sensitivity of these difference ΔnSLD profiles to the magnitude of the translation of the S4 helix within the VSDs. Importantly, our time-resolved neutron interferometry experiments would have been capable of detecting such a smaller translation of the S4 helix within the VSDs of ∼7 Å were it to have occurred in the experimental KvAP-POPC membrane despite the relatively low spatial resolution of the experiment.

Based on the comparisons of the experimental ΔnSLD profile with those for the models of the Kv1.2/2.1 chimera and Kv1.2 noted in the preceding paragraph, our time-resolved neutron interferometry experiments demonstrate directly that the magnitude of the inward translation of the S4 helix upon the transition between the activated, open state and the deactivated, closed state is ∼15 Å for KvAP. The magnitude of the translation associated with this transition for Kv channels has been controversial in the past as reviewed in (3), possibly because of the investigation of different channels in differing environments coupled with the indirect techniques utilized. Nevertheless, there are several such experiments that support a translation of this relatively large magnitude (14,33–35).

CONCLUSIONS

We have demonstrated good agreement between the difference ΔnSLD profile (hyperpolarized minus depolarized) for the experimental KvAP-POPC membrane from our time-resolved neutron interferometry experiments and that for the transmembrane domain of the Kv1.2/2.1 chimera protein embedded within a hydrated POPC bilayer from the MD simulations of (18). This agreement indicates that the inward translation of the S4 helices within the VSDs of KvAP upon the transition between the activated, open state and the deactivated, closed state is ∼15 Å along the membrane profile. We have also demonstrated good agreement between the difference ΔnSLD profile (hyperpolarized minus depolarized) for water within the experimental KvAP-POPC membrane and that for water within the transmembrane domain of the Kv1.2/2.1 chimera protein. Thus, there is a "de-wetting" of the cytoplasmic half of the pore within the PD of KvAP associated with this transition like that predicted from the MD simulations of the Kv1.2/2.1 chimera. The other two fundamentally different computational approaches for modeling these same two states in hydrated phospholipid bilayer membranes were unable to provide agreement with both of these two key results from our time-resolved neutron interferometry experiments.

SUPPORTING MATERIAL

Supporting Material can be found online at https://doi.org/10.1016/j.bpj.2019.07.011.

AUTHOR CONTRIBUTIONS

A.Y.T. performed the experimental measurements (EIS, x-ray interferometry, and time-resolved neutron interferometry). L.J.M., K.C.G., and P.J.L. designed and carried out the expression and purification of the KvAP protein. H.A.A., A.A.P., and V.L. configured the hardware and software associated with the Magnetism Reflectometer at the Spallation Neutron Source to implement the time-resolved "pump-probe" neutron interferometry experiments. A.D.G. manipulated the model proposed for the 3-D structure of KvAP and calculated the corresponding xSLD profiles; constructed the models and performed MD simulations on the activated, open states for the KvAP protein within hydrated POPC bilayers; and performed MD simulations on the activated, open and deactivated, closed states for the Kv1.2 protein within hydrated POPC bilayers. J.A.F. calculated the time-averaged nSLD profiles from the coordinates provided from simulation 6 of the MD simulation for Kv1.2/2.1-T1(−). J.K.B. designed the time-resolved neutron interferometry experiments and analyzed the x-ray and neutron interferometry data. J.K.B., A.D.G., J.A.F., and D.J.T. wrote the manuscript.

ACKNOWLEDGMENTS

We thank Morten Jensen for providing the coordinates from simulation 6 for the Kv1.2/2.1-T1(−) channel within a hydrated POPC bilayer membrane from (18).

Funding was provided by the National Institutes of Health grant P01-GM55876. The Spallation Neutron Source, Oak Ridge National Laboratory, is a user facility sponsored by the Scientific User Facilities Division, Office of Basic Energy Sciences, U.S. Department of Energy. X-ray interferometry measurements were performed at the Multi-Angle X-ray Scattering Facility in the Laboratory for Research on the Structure of Matter, a Materials Research Science and Engineering Center at the University of Pennsylvania funded by the National Science Foundation. MD simulations were performed on the Stampede2 supercomputer at the Texas Advanced Computing Center, University of Texas Austin, funded under the Extreme Science and Engineering Discovery Environment program by the National Science Foundation (grant number ACI-1548562).

SUPPORTING CITATIONS

References (36–50) appear in the Supporting Material.

REFERENCES

1. Hodgkin, A. L. 1951. The ionic basis of electrical activity in nerve and muscle. *Biol. Rev. Camb. Philos. Soc.* 26:339–409.
2. Vargas, E., V. Yarov-Yarovoy, …, B. Roux. 2012. An emerging consensus on voltage-dependent gating from computational modeling and molecular dynamics simulations. *J. Gen. Physiol.* 140:587–594.
3. Grizel, A. V., G. S. Glukhov, and O. S. Sokolova. 2014. Mechanisms of activation of voltage-gated potassium channels. *Acta Naturae.* 6:10–26.
4. Hodgkin, A. L., and A. F. Huxley. 1952. A quantitative description of membrane current and its application to conduction and excitation in nerve. *J. Physiol.* 117:500–544.
5. Long, S. B., X. Tao, …, R. MacKinnon. 2007. Atomic structure of a voltage-dependent K^+ channel in a lipid membrane-like environment. *Nature.* 450:376–382.
6. Payandeh, J., T. Scheuer, …, W. A. Catterall. 2011. The crystal structure of a voltage-gated sodium channel. *Nature.* 475:353–358.
7. Matthies, D., C. Bae, …, K. J. Swartz. 2018. Single-particle cryo-EM structure of a voltage-activated potassium channel in lipid nanodiscs. *eLife.* 7:e37558.
8. Long, S. B., E. B. Campbell, and R. Mackinnon. 2005. Crystal structure of a mammalian voltage-dependent *Shaker* family K^+ channel. *Science.* 309:897–903.
9. Yarov-Yarovoy, V., D. Baker, and W. A. Catterall. 2006. Voltage sensor conformations in the open and closed states in *ROSETTA* structural models of K(+) channels. *Proc. Natl. Acad. Sci. USA.* 103:7292–7297.
10. Pathak, M. M., V. Yarov-Yarovoy, …, E. Y. Isacoff. 2007. Closing in on the resting state of the *Shaker* K(+) channel. *Neuron.* 56:124–140.
11. Khalili-Araghi, F., V. Jogini, …, K. Schulten. 2010. Calculation of the gating charge for the Kv1.2 voltage-activated potassium channel. *Biophys. J.* 98:2189–2198.
12. Schow, E. V., J. A. Freites, …, D. J. Tobias. 2010. Down-state model of the voltage-sensing domain of a potassium channel. *Biophys. J.* 98:2857–2866.
13. Schow, E. V., J. A. Freites, …, D. J. Tobias. 2012. Coupling between the voltage-sensing and pore domains in a voltage-gated potassium channel. *Biochim. Biophys. Acta.* 1818:1726–1736.
14. Henrion, U., J. Renhorn, …, F. Elinder. 2012. Tracking a complete voltage-sensor cycle with metal-ion bridges. *Proc. Natl. Acad. Sci. USA.* 109:8552–8557.
15. Treptow, W., M. Tarek, and M. L. Klein. 2009. Initial response of the potassium channel voltage sensor to a transmembrane potential. *J. Am. Chem. Soc.* 131:2107–2109.
16. Denning, E. J., P. S. Crozier, …, T. B. Woolf. 2009. From the gating charge response to pore domain movement: initial motions of Kv1.2 dynamics under physiological voltage changes. *Mol. Membr. Biol.* 26:397–421.
17. Delemotte, L., M. Tarek, …, W. Treptow. 2011. Intermediate states of the Kv1.2 voltage sensor from atomistic molecular dynamics simulations. *Proc. Natl. Acad. Sci. USA.* 108:6109–6114.
18. Jensen, M. Ø., V. Jogini, …, D. E. Shaw. 2012. Mechanism of voltage gating in potassium channels. *Science.* 336:229–233.
19. Gupta, S., J. Liu, …, J. K. Blasie. 2011. Profile structures of the voltage-sensor domain and the voltage-gated K(+)-channel vectorially oriented in a single phospholipid bilayer membrane at the solid-vapor and solid-liquid interfaces determined by x-ray interferometry. *Phys. Rev. E Stat. Nonlin. Soft Matter Phys.* 84:031911.
20. Blasie, J. K. 2018. 4. Time-resolved neutron interferometry and the mechanism of electromechanical coupling in voltage-gated ion channels. *In* Methods in Enzymology. Volume 603. Chemical and Biochemical Approaches for the Study of Anesthetic Function Part B. R. G. Eckenhoff and I. J. Dmochowski, eds. Elsevier/Academic Press, pp. 67–90.
21. Gupta, S., J. A. Dura, …, J. K. Blasie. 2012. Structural characterization of the voltage-sensor domain and voltage-gated K^+-channel proteins vectorially oriented within a single bilayer membrane at the solid/vapor and solid/liquid interfaces *via* neutron interferometry. *Langmuir.* 28:10504–10520.
22. Krishnan, V., J. Strzalka, …, J. K. Blasie. 2010. Interferometric enhancement of x-ray reflectivity from unperturbed Langmuir monolayers of amphiphiles at the liquid-gas interface. *Phys. Rev. E Stat. Nonlin. Soft Matter Phys.* 81:021604.
23. Tronin, A. Y., C. E. Nordgren, …, J. K. Blasie. 2014. Direct evidence of conformational changes associated with voltage gating in a voltage sensor protein by time-resolved X-ray/neutron interferometry. *Langmuir.* 30:4784–4796.
24. Freites, J. A., E. V. Schow, …, D. J. Tobias. 2012. Microscopic origin of gating current fluctuations in a potassium channel voltage sensor. *Biophys. J.* 102:L44–L46.
25. Schmidt, D., S. R. Cross, and R. MacKinnon. 2009. A gating model for the archeal voltage-dependent K(+) channel KvAP in DPhPC and POPE:POPG decane lipid bilayers. *J. Mol. Biol.* 390:902–912.
26. Weeks, S. D., M. Drinker, and P. J. Loll. 2007. Ligation independent cloning vectors for expression of SUMO fusions. *Protein Expr. Purif.* 53:40–50.
27. Eriks, L. R., J. A. Mayor, and R. S. Kaplan. 2003. A strategy for identification and quantification of detergents frequently used in the purification of membrane proteins. *Anal. Biochem.* 323:234–241.
28. Lauter, V., H. Ambaye, …, A. Parizzi. 2009. Highlights from the magnetism reflectometer at the SNS. *Physica B.* 404:2543–2546.
29. Kneller, L. R., A. M. Edwards, …, J. K. Blasie. 2001. Hydration state of single cytochrome c monolayers on soft interfaces via neutron interferometry. *Biophys. J.* 80:2248–2261.
30. Jiang, Y., A. Lee, …, R. MacKinnon. 2003. X-ray structure of a voltage-dependent K^+ channel. *Nature.* 423:33–41.
31. Lee, S. Y., A. Lee, …, R. MacKinnon. 2005. Structure of the KvAP voltage-dependent K^+ channel and its dependence on the lipid membrane. *Proc. Natl. Acad. Sci. USA.* 102:15441–15446.
32. Lu, Y., M. B. Lerner, …, A. T. C. Johnson. 2012. Graphene-protein bioelectronic devices with wavelength-dependent photoresponse. *Appl. Phys. Lett.* 100:033110.
33. Jiang, Y., V. Ruta, …, R. MacKinnon. 2003. The principle of gating charge movement in a voltage-dependent K^+ channel. *Nature.* 423:42–48.
34. Ruta, V., J. Chen, and R. MacKinnon. 2005. Calibrated measurement of gating-charge arginine displacement in the KvAP voltage-dependent K+ channel. *Cell.* 123:463–475.
35. Tao, X., A. Lee, …, R. MacKinnon. 2010. A gating charge transfer center in voltage sensors. *Science.* 328:67–73.
36. Als-Nielsen, J., D. Jacquemain, …, L. Leiserowitz. 1994. Principles and applications of grazing incidence x-ray and neutron scattering from ordered molecular monolayers at the air-water interface. *Phys. Rep.* 246:251–313.
37. Jo, S., T. Kim, …, W. Im. 2008. CHARMM-GUI: a web-based graphical user interface for CHARMM. *J. Comput. Chem.* 29:1859–1865.
38. Phillips, J. C., R. Braun, …, K. Schulten. 2005. Scalable molecular dynamics with NAMD. *J. Comput. Chem.* 26:1781–1802.
39. MacKerell, A. D., Jr., D. Bashford, …, M. Karplus. 1998. All-atom empirical potential for molecular modeling and dynamics studies of proteins. *J. Phys. Chem. B.* 102:3586–3616.
40. Mackerell, A. D., Jr., M. Feig, and C. L. Brooks, III. 2004. Extending the treatment of backbone energetics in protein force fields: limitations of gas-phase quantum mechanics in reproducing protein conformational distributions in molecular dynamics simulations. *J. Comput. Chem.* 25:1400–1415.
41. Best, R. B., X. Zhu, …, A. D. Mackerell, Jr. 2012. Optimization of the additive CHARMM all-atom protein force field targeting improved sampling of the backbone φ, ψ and side-chain $\chi(1)$ and $\chi(2)$ dihedral angles. *J. Chem. Theory Comput.* 8:3257–3273.
42. Klauda, J. B., R. M. Venable, …, R. W. Pastor. 2010. Update of the CHARMM all-atom additive force field for lipids: validation on six lipid types. *J. Phys. Chem. B.* 114:7830–7843.

43. Jorgensen, W. L., J. Chandrasekhar, …, M. L. Klein. 1983. Comparison of simple potential functions for simulating liquid water. *J. Chem. Phys.* 79:926–935.

44. Martyna, G. J., D. J. Tobias, and M. L. Klein. 1994. Constant-pressure molecular-dynamics algorithms. *J. Chem. Phys.* 101:4177–4189.

45. Feller, S. E., Y. Zhang, …, B. R. Brooks. 1995. Constant pressure molecular dynamics simulation: the Langevin piston method. *J. Chem. Phys.* 103:4613–4621.

46. Ryckaert, J.-P., G. Ciccotti, and H. J. C. Berendsen. 1977. Numerical integration of the Cartesian equations of motion of a system with constraints: molecular dynamics of n-alkanes. *J. Comput. Phys.* 23:327–341.

47. Miyamoto, S., and P. Kollman. 1992. SETTLE: an analytical version of the SHAKE and RATTLE algorithm for rigid water models. *J. Comput. Chem.* 13:952–962.

48. Essmann, U., L. Perera, …, L. G. Pedersen. 1995. A smooth particle mesh Ewald method. *J. Chem. Phys.* 103:8577–8593.

49. Darden, T., D. York, and L. Pedersen. 1993. Particle mesh Ewald: an $N \cdot \log(N)$ method for Ewald sums in large systems. *J. Chem. Phys.* 98:10089–10092.

50. Humphrey, W., A. Dalke, and K. Schulten. 1996. VMD: visual molecular dynamics. *J. Mol. Graph.* 14:33–38, 27–28.

Biophysical Journal, Volume *117*

Supplemental Information

Voltage-Dependent Profile Structures of a Kv-Channel via Time-Resolved Neutron Interferometry

Andrey Y. Tronin, Lina J. Maciunas, Kimberly C. Grasty, Patrick J. Loll, Haile A. Ambaye, Andre A. Parizzi, Valeria Lauter, Andrew D. Geragotelis, J. Alfredo Freites, Douglas J. Tobias, and J. Kent Blasie

Supporting Material:

a) Analysis of the time-resolved neutron interferometry data:

The formalism describing the conventional x-ray or neutron reflectivity experiment was first developed for an amphiphilic macromolecule spread in a Langmuir monolayer at the liquid-gas (e.g., water-helium) interface (1), although it applies to the solid-gas and solid-liquid interfaces as well. Using monochromatic x-rays or neutrons, the reflectivity experiment involves recording the elastically reflected x-rays/neutrons as a function of the angle of incidence (α) which is maintained equal to the angle of reflection (β) for the case of specular reflectivity, both angles measured with respect to the plane of the interface. For the incident x-ray photon/neutron momentum vector $\overrightarrow{k_I}$ and reflected x-ray photon/neutron momentum vector $\overrightarrow{k_R}$, whose magnitudes are each $2\pi/\lambda$ for elastic scattering where λ is the photon/neutron wavelength, the photon/neutron momentum transfer vector for the scattering process is $\overrightarrow{Q_z} = (\overrightarrow{k_R} - \overrightarrow{k_I})$ which is parallel to the normal to the interface $\vec{z}$, where $|\overrightarrow{Q_z}| \equiv Q_z = (4\pi \sin\alpha)/\lambda$. Note that for specular x-ray/neutron reflectivity, $\overrightarrow{k_I}$, $\overrightarrow{k_R}$ and $\overrightarrow{Q_z}$ all lie in the same plane perpendicular to the interface. In this formalism, the Fresnel-normalized reflectivity $R(Q_z)/R_F(Q_z)$ is defined as the specular reflectivity $R(Q_z)$ divided by that from an ideal (flat and smooth) interface $R_F(Q_z)$ described by an analytic function. Furthermore, the Fresnel-normalized reflectivity $R(Q_z)/R_F(Q_z) = |F(Q_z')|^2$, where $F(Q_z') \equiv \frac{1}{\rho_{ave}} \int \frac{d\rho(z)}{dz} e^{iQ_z'z} dz$ and $(Q_z')^2 = \{(Q_z)^2 - sign(\rho_{ave})(Q_z)_{crit}^2\}$ with $(Q_z)_{crit}$ defined as Q_z at the critical angle for reflection. In this formalism developed in the Born approximation for elastic x-ray/neutron scattering, $F(Q_z')$ is proportional to the Fourier transform of the *gradient* of the scattering-length density profile $d\rho(z)/dz$. In general, $F(Q_z') = |F(Q_z')|e^{i\phi(Q_z')}$ where $|F(Q_z')|$ is the modulus and $\phi(Q_z')$ is the phase of the Fourier transform, the latter being lost upon recording the Fresnel-normalized reflectivity data $R(Q_z)/R_F(Q_z)$. This missing phase information must be recovered in order to unambiguously derive the *gradient* of the SLD profile $d\rho(z)/dz$ from the data, and hence the scattering-length density profile itself, $\rho(z)$, via integration. Note that in this formalism, with $F(Q_z')$ defined as the Fourier transform (FT) of the gradient SLD profile $d\rho(z)/dz$, then $d\rho(z)/dz$ is the inverse Fourier transform (FT^{-1}) of $F(Q_z')$, where both transforms are mathematically unique. Interferometry is a well-developed method for recovering this missing phase information that employs a so-called inorganic multilayer *reference* structure positioned sufficiently near the bio-organic ultrathin film, including immediately adjacent, for the interference effect to occur (2). Its application for the neutron case, using the above formalism, has been thoroughly documented in numerous references, beginning with reference (3). Our approach utilizes a constrained refinement to determine the unknown phase information, which is particularly well-suited to this formalism as described below. Briefly, $d\rho(z)/dz$ is of finite extent Δ, i.e., it is bounded, for an ultrathin bio-organic film with an adjacent inorganic multilayer at either the solid-liquid or the solid-gas interface because the SLD, $\rho(z)$, itself becomes constant for distances along the interface normal sufficiently far from the film. As a result, the autocorrelation of $d\rho(z)/dz$, namely $\left\{\frac{d\rho(z)}{dz} * \frac{d\rho(-z)}{dz}\right\}$, which can be obtained from the inverse Fourier transform of the data $R(Q_z)/R_F(Q_z) = |F(Q_z')|^2$ without any phase information, is similarly of finite extent 2Δ, possessing no information content for $|z| > \Delta$, thereby providing a key constraint on the to-be-derived gradient SLD profile. Since the SLD, $\rho(z)$, of the inorganic multilayer reference structure is essentially known from its fabrication

specifications, as can be confirmed by x-ray reflectivity in the absence of the adjacent bio-organic film, the phase of the Fourier transform of its gradient SLD profile $d\rho(z)/dz$ is also known by simple calculation. The constrained refinement is initiated, utilizing an inverse Fourier transform (FT^{-1}) of the experimental $|F(Q_z')|$ modulus data for the ultrathin bio-organic film adjacent the inorganic multilayer reference structure combined with the known phase of the reference structure's gradient SLD profile to calculate the first approximation to the gradient SLD profile for the ultrathin bio-organic film adjacent the inorganic multilayer reference structure. The key constraint is then applied by truncating this first approximation to the gradient SLD profile for $|z| > \Delta/2$ and a new phase function $\phi(Q_z')$ is created for the so-truncated gradient SLD profile via Fourier transformation (FT), which is then combined with the experimental $|F(Q_z')|$ modulus data for the ultrathin bio-organic film adjacent the inorganic multilayer reference structure to calculate the second approximation to the gradient SLD profile via inverse Fourier transformation (FT^{-1}). This process is then repeated until convergence is achieved, usually within less than 10 iterations. The converged gradient SLD profile $d\rho(z)/dz$ is then simply integrated to provide the SLD itself, $\rho(z)$.

There is a further consideration with regard to the formalism developed in reference (1), which is important to the "pump-probe" neutron interferometry approach described below. The reflectivity itself, $R(Q_z)$ decays over six to seven orders of magnitude with increasing momentum transfer Q_z (4). The Fresnel function $R_F(Q_z)$ is a precise analytic function, and hence division by the Fresnel function to result in the Fresnel-normalized reflectivity $R(Q_z)/R_F(Q_z)$ has no effect on the statistical accuracy inherent in the reflectivity data. However, the normalization does result in the Fresnel-normalized reflectivity being of comparable amplitude over the entire range of momentum transfer Q_z accessed in the experiment. Since the changes in the membrane nSLD profile $\rho(z)$, which are dependent on the applied transmembrane voltage, are expected to be relatively small due to the nature of the profile projection, the Fresnel normalization of the reflectivity data makes it much less difficult to readily ascertain whether the voltage-induced changes are statistically significant.

(b) Specimen-to-specimen reproducibility:

Four different KvAP-POPC membrane specimens were investigated that differed slightly in terms of the separation between the membrane and the surface of the SiGeSi multilayer substrate at the 1-2Å level, and the Fresnel-normalized neutron interferometry data, $R(Q_z)/R_F(Q_z)$, are exquisitely sensitive to this separation. Thus, it might appear that specimen-to-specimen reproducibility in terms of their dependence on the transmembrane voltage could only be ascertained from a complete analysis of the data through to the nSLD profiles for the membrane itself, which includes recovering the otherwise missing phase information, as opposed to a simple inspection of their respective $R(Q_z)/R_F(Q_z)$ data. However, the autocorrelation of $d\rho(z)/dz$, namely $\left\{\frac{d\rho(z)}{dz} * \frac{d\rho(-z)}{dz}\right\}$, can be obtained from the inverse Fourier transform of the data $R(Q_z)/R_F(Q_z) = |F(Q_z')|^2$ *without any phase information*, as described in section (a) above, and can thereby provide a different assessment as to whether the four specimens investigated exhibit any significant dependence on the transmembrane voltage. Figure SM 2 contains the autocorrelation functions calculated for the four specimens investigated S2-S5, along with that of the control specimen S1 comprised of only the Si-Ge-Si multilayer substrate and the organic self-assembled monolayer used to tether the KvAP channel protein to the surface of specimens S2-S5, all at a contrast provided by 90%D_2O/10%H_2O. As can be seen, the autocorrelation function

for S1 contains significant larger amplitude fluctuations only for $|z| < 100$Å, the smaller amplitude fluctuations for larger z-values arising from truncation of the inverse Fourier transform at the maximum value of Q_z accessed, namely ~ 0.2Å^{-1}. For specimens S2-S5, the autocorrelation functions contain significant larger amplitude fluctuations extending further out to $|z|$ ~ 200Å due to the presence of the KvAP-POPC membrane on their surface, and only smaller amplitude fluctuations for larger z-values arising from truncation of the inverse Fourier transform. Using for reference the minimal voltage dependence exhibited by specimen S1 lacking the KvAP-POPC membrane for $|z| < 200$Å, specimens S2 and S5 show a substantial dependence on the transmembrane voltage extending over the entire range for $|z| < 200$Å, and particularly in that region due to the presence of the membrane on the multilayer substrate's surface for 100Å < $|z|$ < 200Å. Specimens S3 and S4 show a distinctly smaller dependence on the transmembrane voltage over the entire range for $|z| < 200$Å, the voltage dependence essentially only appearing in that region due to the presence of the membrane on the multilayer substrate's surface nearer the boundary of the autocorrelation function, namely for ~ 140Å < $|z|$ < 200Å. On this basis, two of the four KvAP-POPC membrane specimens exhibit a substantial dependence on the transmembrane voltage while the other two exhibit a smaller dependence on the transmembrane voltage, but still not approaching that of the control specimen lacking the membrane. Not surprisingly in view of the above, like the $R(Q_z)/R_F(Q_z)$ data shown in Figure 3 for specimen S2, the $R(Q_z)/R_F(Q_z)$ data for specimen S5 also show experimentally significant differences in the mean of the $R(Q_z)/R_F(Q_z)$ data that exceed the standard errors consistently over small ranges of momentum transfer Q_z for both contrasts, becoming progressively more evident with increasing Q_z, and being somewhat larger for 60%D_2O/40%H_2O. On the other hand, while the $R(Q_z)/R_F(Q_z)$ data for specimens S3 and S4 do show differences in the mean of the $R(Q_z)/R_F(Q_z)$ data over small ranges of momentum transfer Q_z, these differences do not exceed the standard errors, i.e., the errors overlap. As a result of the above considerations of both the $R(Q_z)/R_F(Q_z)$ data and their respective inverse Fourier transforms, the autocorrelation functions, the dependence of both specimens S2 and S5 on the transmembrane voltage is clearly experimentally significant, while that for specimens S3 and S4 is more difficult to establish.

The *difference* ΔnSLD profiles at the two contrasts for the KvAP-POPC membrane of specimen S5 were entirely similar and of comparable amplitude to those shown in Figure 3 for specimen S2. Despite the difficulty in establishing the experimental significance of the dependence of specimens S3 and S4 on the transmembrane voltage noted at the end of the preceding paragraph, the changes in the *difference* ΔnSLD profiles for these two specimens were very similar to those for specimens S2 and S5, but smaller in amplitude by a factor of 2, thereby likely explaining the difficulty noted.

(c) Molecular dynamics simulations:

Kv1.2/2.1: For the Kv1.2/2.1 chimera channel embedded within a POPC bilayer, details of the long MD simulation trajectories in which both large depolarizing transmembrane voltages and subsequently large hyperpolarizing transmembrane voltages were applied to the membrane are provided in reference (5), and the corresponding Supplemental Information. With reference to Figure 1 in reference (5), the authors provided coordinates from "simulation 6" for the transmembrane domain of the Kv1.2/2.1 chimera channel, designated as Kv1.2/2.1-T1(-), sampled at intervals of 2.2 μs over the 220 μs trajectory. This sampling provided only six instantaneous configurations for the activated, open (depolarized) state of the channel from the

first 13.2 μs of the trajectory. For consistency, we selected only six instantaneous configurations over the last 13.2 μs of the trajectory for the deactivated, closed (hyperpolarized) state of the channel. For the membrane, the atom selection included the protein, water and lipid within the entire MD cell of dimensions 125Å x 125Å x 145Å. Each selected atom was binned into 0.5 Å steps along the transmembrane-axis for each of the sampled configurations. The neutron atomic scattering lengths were summed for each bin and these values were averaged over all 6 configurations to construct the time-averaged nSLD profile for each state of the Kv1.2/2.1 chimera channel. The origin was defined as the protein center of mass for each configuration. Different deuteration ratios were achieved by randomly selecting a fraction of the hydrogen atoms on water and polar hydrogens on the protein to replace with deuterium. The same approach was employed to calculate the separate time-averaged nSLD profiles for the protein, lipid and water components of the membrane as determined by the atom selection.

Kv1.2: Initial structures for the activated, open and deactivated, closed states of Kv1.2 were based on the models originally obtained via ROSETTA membrane protein structure prediction (6) and subsequently refined by molecular dynamics (MD) simulation in a hydrated POPC bilayer membrane environment coupled with experimental restraints (7). The cytoplasmic T1 domain was removed at residue 150 to provide just the transmembrane domain of the Kv1.2 channel, thereby including residues 151 to 421. Three of the crystallographic potassium ions from (8) in sites S1 and S3 of the selectivity filter and one in the internal vestibule were included in the simulations. The protein was solvated with POPC lipid molecules using the CHARMM-GUI (9), then placed in a water box of dimensions 120Åx120Åx100Å, and KCl was added to neutralize the system and set an ion concentration of 150 mM using the VMD Autoionize plugin. The final system had 140,889 atoms for the deactivated, closed state and 144,944 atoms for the activated, open state.

MD simulations were performed using NAMD software version 2.11 (10) with the CHARMM36 forcefield for the protein and lipids (11-14) and TIP3P waters (15). The simulations used a 2 fs timestep with a Langevin dynamics scheme for temperature control and the Nosé-Hoover Langevin piston for pressure control (16-17). Lengths of bonds involving hydrogen were fixed using the SHAKE (18) and SETTLE (19) algorithms. The smooth particle mesh Ewald method (20-21) was used to calculate electrostatic interactions with a cut-off at 11 Å, employing a switching function. Visualization and analysis of the trajectories were performed using VMD (22).

After 10,000 steps of minimization, the Kv1.2 systems were run in the NVT ensemble at 300 K for 2 ns with the protein held fixed. They were then run in the NPT ensemble at 300 K and 1 atm for 2 ns with harmonic restraints on the protein heavy atom positions using a force constant of 1.5 kcal/mol/Å^2. The protein restraints were removed over 1 ns. Both systems were then run in the NPT ensemble at 300 K and 1 atm for 55 ns. Harmonic restraints were placed on the three selectivity-filter potassium ions for the entire simulation with a force constant of 1 kcal/mol/Å^2.

We applied a depolarizing transmembrane voltage of 150 mV for the activated, open state and polarizing transmembrane voltage of -150 mV for the deactivated, closed state by applying a constant electric field along the transmembrane direction. Given the magnitudes of these voltage gradients and the very short lengths (55 ns) of the MD trajectories compared with those required to actually change the conformation of the Kv-channel (e.g., see reference (5)), the voltage gradients were only intended to help stabilize the respective states of the Kv-channel within the

hydrated bilayer membrane. The deactivated, closed state simulation had two additional restraints to ensure the pore remained closed. The first was a distance restraint between alpha-carbon atoms on residue 410 for opposing subunits. A harmonic potential, with a force constant of 5 kcal/mol/Å^2, was applied if the distance between the alpha-carbon atoms was greater than 11.5 Å. To maintain the alpha-helical secondary structure for the S6 helix, harmonic restraints with a force constant of 200 kcal/mol were applied to the helix backbone phi and psi dihedral angles. This was done using the Extrabonds feature in NAMD.

The last 50 ns of the trajectories for the activated, open and deactivated, closed states of Kv1.2 in the hydrated POPC bilayer were sampled at 100 ps intervals to generate 500 instantaneous configurations of the system used to calculate the time-averaged nSLD profiles. For the membrane, the atom selection included the protein, water and lipid within a cylinder of radius 50 Å extending outward from the center of the protein perpendicular to the transmembrane-axis. Each selected atom was binned into 0.5 Å steps along the transmembrane-axis for each of the sampled configurations. The neutron atomic scattering lengths were summed for each bin and these values were averaged over all 500 configurations to construct the time-averaged nSLD profile for each state of the Kv1.2 protein. The origin was defined as the protein center of mass for each configuration. Different deuteration ratios were achieved by randomly selecting a fraction of the hydrogen atoms on water and polar hydrogens on the protein to replace with deuterium. The same approach was employed to calculate the separate time-averaged nSLD profiles for the protein, lipid and water components of the membrane as determined by the atom selection.

KvAP: An improved model for the activated, open state of the KvAP protein within a hydrated POPC bilayer was constructed with respect to that in reference (23). The model was constructed by splicing the activated state of the VSDs, obtained from a 10μs MD simulation of the isolated VSD within a hydrated POPC bilayer at a depolarizing transmembrane voltage of 120mV (24-25) in which the S4 helix was in its outwardmost position, onto the presumed activated, open state of the pore domain (PD) obtained from a MD simulation of the complete homo-tetrameric KvAP within a hydrated POPC bilayer at a non-polarizing transmembrane voltage of 0mV (23). The VSD consisted of residues 24-147 and the PD contained residues 148-240. The splicing was accomplished by replacing the presumed activated VSDs (unpolarized) of the complete homo-tetrameric KvAP with the activated VSDs (depolarized) after aligning the Cα-atoms of only the S1 and S2 helices and then making minor manual adjustments to avoid overlap between the activated VSDs and the open PD. POPC lipids, waters, and ions were retained from the complete channel simulation (23). Following deletion of overlapping molecules, 50,000 steps of energy minimization were performed. The system dimensions were 165Åx165Åx100Å and contained 256,669 atoms in total: 13,832 protein atoms, 47,129 TIP3P waters, 755 POPC lipid molecules, 136 K^+ ions, and 144 Cl^- ions.

A MD simulation, otherwise similar to that described above for Kv1.2, was run in the NPT ensemble at 1 atm and 300 K with a depolarizing transmembrane voltage of 150mV to help stabilize the activated state of the VSDs. The protein heavy atoms were held fixed for 6 ns, followed by harmonic restraints on atom positions using a force constant of 10 kcal/mol/Å^2 for 8 ns, followed by harmonic restraints on just the protein backbone atom positions with a force constant of 1 kcal/mol/Å^2 for 20 ns. The last 10 ns of this restrained trajectory was sampled at 20ps intervals to generate 500 instantaneous configurations of the system used to calculate the time-averaged nSLD profiles. Note that the activated (depolarized) state of the VSD in the

simulation in reference (24) was stable over the last 5μs of the 10μs trajectory following application of the depolarizing transmembrane voltage. Thus, despite the short length of the restrained trajectory, this sampling was deemed sufficient because its primary purpose was to allow for the relaxation of the lipid and water molecules in response to embedding this activated, open (depolarized) state of the KvAP protein in the POPC bilayer.

The structure for the deactivated, closed state of KvAP was taken directly from the targeted MD simulation of reference (23). Following removal of the targeting restraints used to induce this state, the trajectory was continued unrestrained under a polarizing transmembrane voltage of -100mV for 280ns. The unrestrained trajectory was sampled at 5ns sampling intervals to generate 56 instantaneous configurations of the system used to calculate the time-averaged nSLD profiles.

For both the activated, open (depolarized) and deactivated, closed (polarized) states of the KvAP protein in the hydrated POPC bilayer, the atom selection for the nSLD profiles included the protein, water and lipid within a cylinder of radius 44 Å extending outward from the center of the protein perpendicular to the transmembrane-axis. This selection yielded a molar ratio of about 130 POPC:1 KvAP, approximately that for the experimental KvAP-POPC membrane. Each selected atom was binned into 0.5 Å steps along the transmembrane-axis for each of the sampled configurations. The neutron atomic scattering-lengths were summed for each bin and these values were averaged over all of the sampled configurations to construct the time-averaged nSLD profile for each state of the KvAP protein. The origin was defined as the protein center of mass for each sampled configuration. Different deuteration ratios were achieved by randomly selecting a fraction of the hydrogen atoms on water and polar hydrogens on the protein to replace with deuterium. The same approach was employed to calculate the separate time-averaged nSLD profiles for the protein, lipid and water components of the membrane as determined by the atom selection.

(d) Effect of the spatial resolution on detecting smaller translations of the S4 helix:

With respect to the three main features in the experimental *difference* ΔnSLD profile (hyperpolarized - depolarized) at a contrast of 60%D_2O in Figure 7A, the larger maximum occurs near the cytoplasmic surface of the membrane separated from a second maximum within the cytoplasmic half of the membrane by 28Å while the minimum occurs within the extracellular half of the membrane separated from the first maximum by 50Å. The two separations of these three main features are the only unique attributes of the experimental ΔnSLD profile. The experimental nSLD profile for the KvAP-POPC membrane is dominated by the KvAP protein. As a result, it is notable that the ΔnSLD profiles for both the simulated Kv1.2/2.1 chimera protein and the simulated Kv1.2 protein within their respective POPC bilayer membranes exhibit the same three features, namely two maxima and one minimum that span their respective membrane profiles. From Table 1 in the main manuscript, the two unique separations for the ΔnSLD profile of the Kv1.2/2.1 chimera protein match those of the experimental KvAP-POPC membrane to within less than 1Å. However, the two unique separations for the ΔnSLD profile of the Kv1.2 protein are 6-8Å smaller than those for the experimental KvAP-POPC membrane. Hence, the question arises as to whether our time-resolved neutron interferometry experiments could have detected these smaller separations given the relatively low spatial-resolution of the experimental nSLD profiles for the KvAP-POPC membrane at hyperpolarizing and depolarizing transmembrane voltages.

To address this important issue, slab models (4) were generated for the nSLD profiles of the experimental KvAP-POPC membrane, based on a finite sum of error functions and designated as Model 1 in Figure SM 4A. Least-squares fitting was employed to match the features of the experimental nSLD profiles for the membrane at both a depolarizing transmembrane voltage of -20mV and a hyperpolarizing voltage of +150mV, as well as the features of the modulus square of the Fourier transform of the gradient nSLD profiles, the experimental Fresnel-normalized neutron reflectivity. The *difference* ΔnSLD profile (hyperpolarized - depolarized) for the slab models is shown in Figure SM 4C. The corresponding resolution-limited nSLD profile for Model 1 in Figure SM 4B was calculated via Fourier transformation of its gradient nSLD profile into momentum transfer space (Q_z), followed by inverse Fourier transformation back into real space (z) at the experimental resolution defined by the maximum value of Q_z to which the experimental Fresnel-normalized neutron reflectivity was observed. This was followed by integration to produce the resolution-limited nSLD profiles. The difference (hyperpolarized - depolarized) of these resolution-limited profiles produced the ΔnSLD profile shown in the Figure SM 4D. Since the largest feature in the experimental ΔnSLD profile occurs near the cytoplasmic surface of the membrane, we decided to investigate the effect of the experimental spatial resolution on our ability to detect translations of the cytoplasmic interface in Model 1 toward the centroid of the membrane nSLD profile, while maintaining all other features constant. Two additional slab models were generated in which the translation was 8Å for Model 2 and 12Å for Model 3. The resolution-limited nSLD profiles were calculated for Models 2 and 3 as described above for Model 1, followed by calculation of the corresponding difference ΔnSLD profiles shown in the Figure SM 4E. As evident in Figure SM 4E, the first maximum near the cytoplasmic surface remains distinguishable from the second maximum for both Model 2 and Model 3 at the experimental spatial-resolution. From the parameter Table in Figure SM 4, the two unique parameters for the ΔnSLD profile of Model 2 are 2Å larger than for the ΔnSLD profile of the Kv1.2 protein while those for the ΔnSLD profile of Model 3 are 1-2Å smaller than those for the Kv1.2 protein. Thus, it appears that a translation of the cytoplasmic interface by ~10Å would have matched the parameters for the ΔnSLD profile for the Kv1.2 protein, while no translation represented by the ΔnSLD profile for Model 1 matches the parameters for both the Kv1.2/2.1 chimera protein and the KvAP protein. The ΔnSLD profiles for both the Kv1.2/2.1 protein and the Kv1.2 protein are dominated by the VSDs throughout the membrane profile, although the PD also makes a contribution near the cytoplasmic surface of the membrane, as shown for the Kv1.2/2.1 chimera protein in Figure SM 3. Thus, the smaller translation of ~7Å for the S4-helix within the VSDs of Kv1.2 would have indeed been distinguishable from the larger translation of ~15Å for the S4-helix within the VSDs for Kv1.2/2.1, given the experimental spatial-resolution of the nSLD profiles for the KvAP-POPC membrane (hyperpolarized and depolarized).

Supporting Material References:

(1) Als-Nielsen, J., D. Jacquemain, K. Kjaer, F. Leveiller, M. Lahav, and L. Leiserowitz. 1994. Principles and applications of grazing incidence x-ray and neutron scattering from ordered molecular monolayers at the air-water interface. Phys. Rep. 246:251-313.

(2) Krishnan, V., J. Strzalka, J. Liu, C. Liu, I. Kuzmenko, T. Gog, and J.K. Blasie. 2010. Interferometric enhancement of x-ray reflectivity from unperturbed Langmuir monolayers of amphiphiles at the liquid-gas interface. Phys. Rev. E 81:021604-1-10.

(3) Kneller, L.R., A.M. Edwards, C.F. Majkrzak, N.F. Berk, S. Krueger, and J.K. Blasie. 2001. Hydration state of a single cytochrome c monolayer vectorially-oriented at a soft interface investigated via neutron interferometry. Biophys. J. 80(5):2248-2261.

(4) Gupta, S., J. Dura, A. Freites, D. Tobias, and J.K. Blasie. 2012. Structural characterization of the voltage sensor domain and voltage-gated K^+-channel proteins vectorially-oriented within a single bilayer membrane at the solid/vapor and solid/liquid interfaces *via* neutron interferometry. Langmuir 28(28):10504-10520.

(5) Jensen, M.Ø., V. Jogini, D.W. Borhani, A.E. Leffler, R.O. Dror, and D.E. Shaw. 2012. Mechanism of voltage gating in potassium channels. Science 336:229-233.

(6) Yarov-Yarovoy, V., D. Baker, and W.A. Catterall. 2006. Voltage sensor conformations in the open and closed states in *ROSETTA* structural models of K^+ channels. Proc. Nat. Acad. Sci. USA. 103(19):7292-7297.

(7) Pathak, M.M., V. Yarov-Yarovoy, G. Agarwal, B. Roux, P. Barth, S. Kohout, F. Tombola, and E.Y. Isacoff. 2007. Closing in on the resting state of the Shaker K^+ channel. Neuron. 56:124-140.

(8) Long, S.B., E.B. Campbell, and R. MacKinnon. 2005. Crystal structure of a mammalian voltage-dependent *Shaker* family K^+ channel. Science. 309:897-903.

(9) Jo, S., T. Kim, V.G. Iyer, and W. Im. 2008. CHARMM-GUI: a web-based graphical user interface for CHARMM. J. Comput. Chem. 29:1859-1865.

(10) Phillips, J.C., R. Braun, W. Wang, J. Gumbart, E. Tajkhorshid, E. Villa, C. Chipot, R.D. Skeel, L. Kalé, and K. Schulten. 2005. Scalable molecular dynamics with NAMD. J. Comput. Chem. 26:1781-1802.

(11) MacKerell, Jr., A.D., D. Bashford, M. Bellott, R.L. Dunbrack, J.D. Evanseck, M.J. Field, S. Fischer, J. Gao, H. Guo, S. Ha, D. Joseph-McCarthy, L. Kuchnir, K. Kuczera, F.T. Lau, C. Mattos, S. Michnick, T. Ngo, D.T. Nguyen, B. Prodhom, W.E. Reiher, B. Roux, M. Schlenkrich, J.C. Smith, R. Stote, J. Straub, M. Watanabe, J. Wiórkiewicz-Kuczera, D. Yin, and M. Karplus. 1998. All-atom empirical potential for molecular modeling and dynamics studies of proteins. J. Phys. Chem. B. 102:3586-3616.

(12) MacKerell, Jr., A.D., M. Feig, and C.L. Brooks, III. 2004. Extending the treatment of backbone energetics in protein force fields: limitations of gas-phase quantum mechanics in reproducing protein conformational distributions in molecular dynamics simulations. J. Comput. Chem. 25: 1400-1415.

(13) Best, R.B., X. Zhu, J. Shim, P.E.M. Lopes, J. Mittal, M. Feig, and A.D. MacKerell Jr. 2012. Optimization of the additive CHARMM all-atom protein force field targeting improved sampling of the backbone phi, psi and side-chain chi1 and chi2 dihedral angles. J. Chem. Theory Comput. 8:3257-3273.

(14) Klauda, J.B., R.M. Venable, J.A. Freites, J.W. O'Connor, D.J. Tobias, C. Mondragon-Ramirez, I. Vorobyov, A.D. MacKerell Jr., and R.W. Pastor. 2010. Update of the CHARMM all-atom additive force field for lipids: validation on six lipid types. J. Phys. Chem. B. 114:7830–7843.

(15) Jorgensen, W.L., J. Chandrasekhar, J.D. Madura, R.W. Impey, and M.L. Klein. 1983. Comparison of simple potential functions for simulating liquid water. J. Chem. Phys. 79:926–935.

(16) Martyna, G.J., D.J. Tobias, and M.L. Klein. 1994. Constant-pressure molecular-dynamics algorithms. J. Chem. Phys. 101:4177-4189.

(17) Feller, S.E., Y. Zhang, R.W. Pastor, and B.R. Brooks. 1995. Constant pressure molecular dynamics simulation: the Langevin piston method. J. Chem. Phys. 103:4613-4621.

(18) Ryckaert, J.-P., G. Ciccotti, and H.J.C. Berendsen. 1977. Numerical integration of the Cartesian equations of motion of a system with constraints: molecular dynamics of n-alkanes. J. Comput. Phys. 23:327-341.

(19) Miyamoto, S., and P. Kollman. 1992. An analytical version of the SHAKE and RATTLE algorithm for rigid water models. J. Comput. Chem. 13:952-962.

(20) Essmann, U., L. Perera, M.L. Berkowitz, T. Darden, H. Lee, and L.G. Pedersen. 1995. A smooth particle mesh Ewald method. J. Chem. Phys. 103:8577–8593.

(21) Darden, T., D. York, and L. Pedersen. 1993. Particle mesh Ewald: an $N\cdot\log(N)$ method for Ewald sums in large systems. J. Chem. Phys. 98:10089-10092.

(22) Humphrey, W., A. Dalke, and K. Schulten. 1996. VMD: visual molecular dynamics. J. Mol. Graph. 14:33-38, 27-28.

(23) Schow, E.V., J.A. Freites, A. Nizkorodov, S.H. White, D.J. Tobias. 2012. Coupling between the voltage-sensing and pore domains in a voltage-gated potassium channel. Biochim. Biophys. Acta. 1818:1726-1736.

(24) Freites, J.A., E.V. Schow, S.H. White, and D.J. Tobias. 2012. Microscopic Origin of Gating Current Fluctuations in a Potassium Channel Voltage Sensor. Biophys. J. 102:L44-L46.

(25) Tronin, A., J.W. Strzalka, I. Kuzmenko, D. Worcester, V. Lauter, J.A. Freites, D.J. Tobias, and J.K. Blasie. 2014. Direct evidence of conformational changes associated with voltage-gating in a voltage sensor protein by time-resolved x-ray/neutron interferometry. Langmuir 30(16):4784-4796.

Supporting Material Figure Legends:

Figure SM 1: Typical Electrical Impedance Spectroscopy (EIS) data shown as Nyquist plots.
(A) The SAM (circles) on a monolayer graphene on Si-Ge-Si substrate.
(B) The KvAP-POPC membrane (circles) on the same monolayer graphene on Si-Ge-Si substrate.
(C) The KvAP-POPC membrane (circles) on a Si-Ge-Si substrate.
The best model fits to the respective EIS data (red) utilized one R-RC circuit to represent the substrate and a second RC circuit in series to represent the bio-organic overlayer on its surface. The EIS data were acquired using a CHI660D Electrochemical Workstation (CH Instruments). The electrochemical cell was either that used in the time-resolved neutron interferometry experiments or a similar cell to accommodate the smaller area (e.g., 1 x 2cm^2) of the substrates employed in the x-ray interferometry experiments.

Figure SM 2: Autocorrelation functions $\left\{\frac{d\rho(z)}{dz} * \frac{d\rho(-z)}{dz}\right\}$.
The autocorrelation functions for the hyperpolarizing transmembrane voltage are shown in blue and those for the depolarizing voltage are shown in red. For clarity, the ordinate and abscissa are labeled only for the specimen S1 SAM in Panel (E).
(A) Specimen S2 KvAP:POPC membrane at a contrast of 90% D_2O/10% H_2O.
(B) Specimen S5 KvAP:POPC membrane at a contrast of 90% D_2O/10% H_2O.
(C) Specimen S4 KvAP:POPC membrane at a contrast of 90% D_2O/10% H_2O.
(D) Specimen S3 KvAP:POPC membrane at a contrast of 90% D_2O/10% H_2O.
(E) Specimen S1 SAM at a contrast of 90% D_2O/10% H_2O.

Figure SM 3: Decomposition of the ΔnSLD(z) profile (hyperpolarized – depolarized) for the transmembrane domain of the Kv1.2/2.1 chimera.
(Blue)- ΔnSLD(z) profile for the transmembrane domain of the Kv1.2/2.1 protein within a hydrated POPC bilayer from Figure 7.
(Green)- ΔnSLD(z) profile for only the VSDs within the transmembrane domain of the Kv1.2/2.1 protein.
(Red)- ΔnSLD(z) profile for only the PD within the transmembrane domain of the Kv1.2/2.1 protein.

Figure SM 4: Modeling the three main features in the *difference* ΔnSLD profile (hyperpolarized – depolarized) for KvAP.
(A) Slab model (Model 1) profiles for the nSLD(z) profiles of the experimental KvAP-POPC membrane at a contrast of 60% D_2O/40% H_2O (hyperpolarized, blue; depolarized, red).
(B) Resolution-limited nSLD(z) profiles calculated for the Model 1 profiles in (A) at the spatial-resolution of the experiment.
(C) The *difference* ΔnSLD(z) profile (hyperpolarized-depolarized) for the slab model (Model 1) profiles in (A).
(D) The *difference* ΔnSLD(z) profile (hyperpolarized-depolarized) for the resolution-limited nSLD(z) profiles in (B).
(E) Comparison of the resolution-limited ΔnSLD(z) profiles for slab Model 1 (black) with those for slab models in which the cytoplasmic interface in panel (A) is shifted by 8Å (Model 2,

magenta) or 12Å (Model 3, turquoise) toward the centroid of the membrane nSLD profile at ~75Å.

(Table) The two unique separations of the three main features in ΔnSLD profiles are compared for the KvAP protein within the experimental KvAP-POPC membrane, for the Kv1.2/2.1 chimera protein within the simulated Kv1.2/2.1-POPC membrane, for the Kv1.2 protein within the simulated Kv1.2-POPC membrane, and for the resolution-limited Models 1-3.

Figure SM 1:

(A) SAM on Graphene

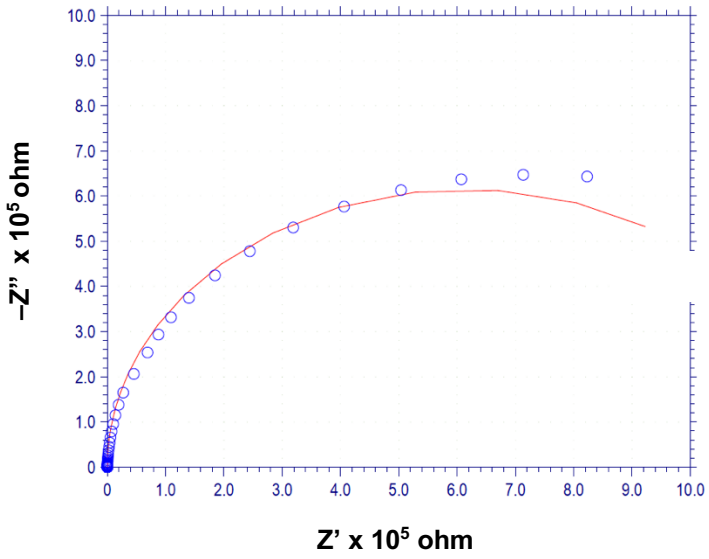

(B) KvAP-POPC on Graphene

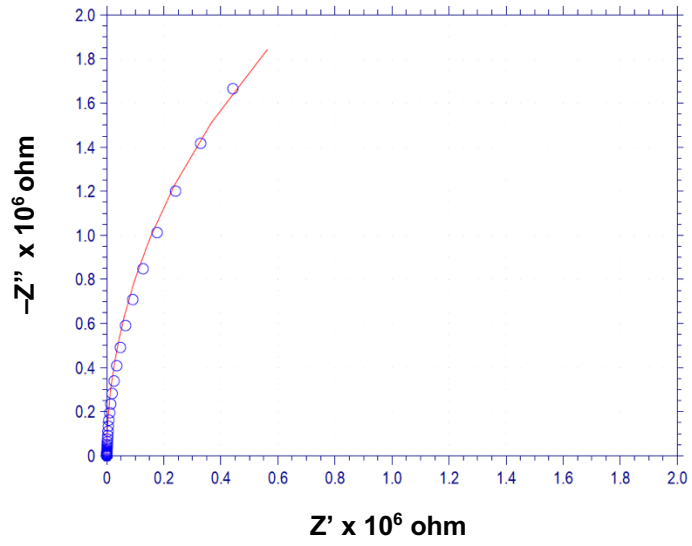

(B) KvAP-POPC on Silicon

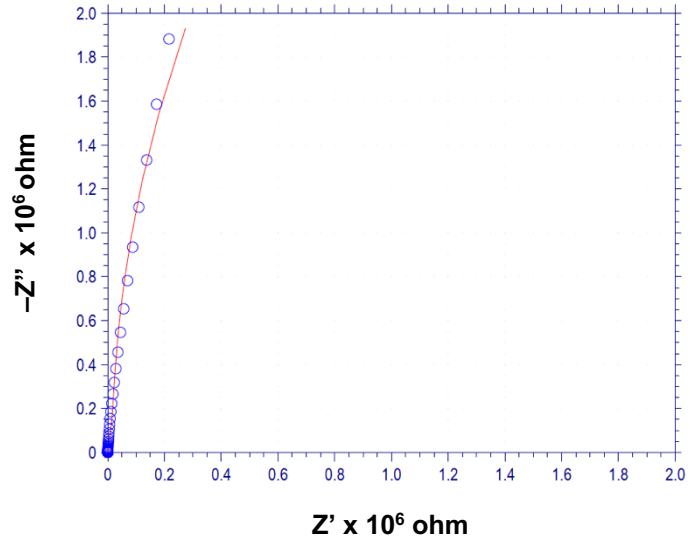

Figure SM 2:

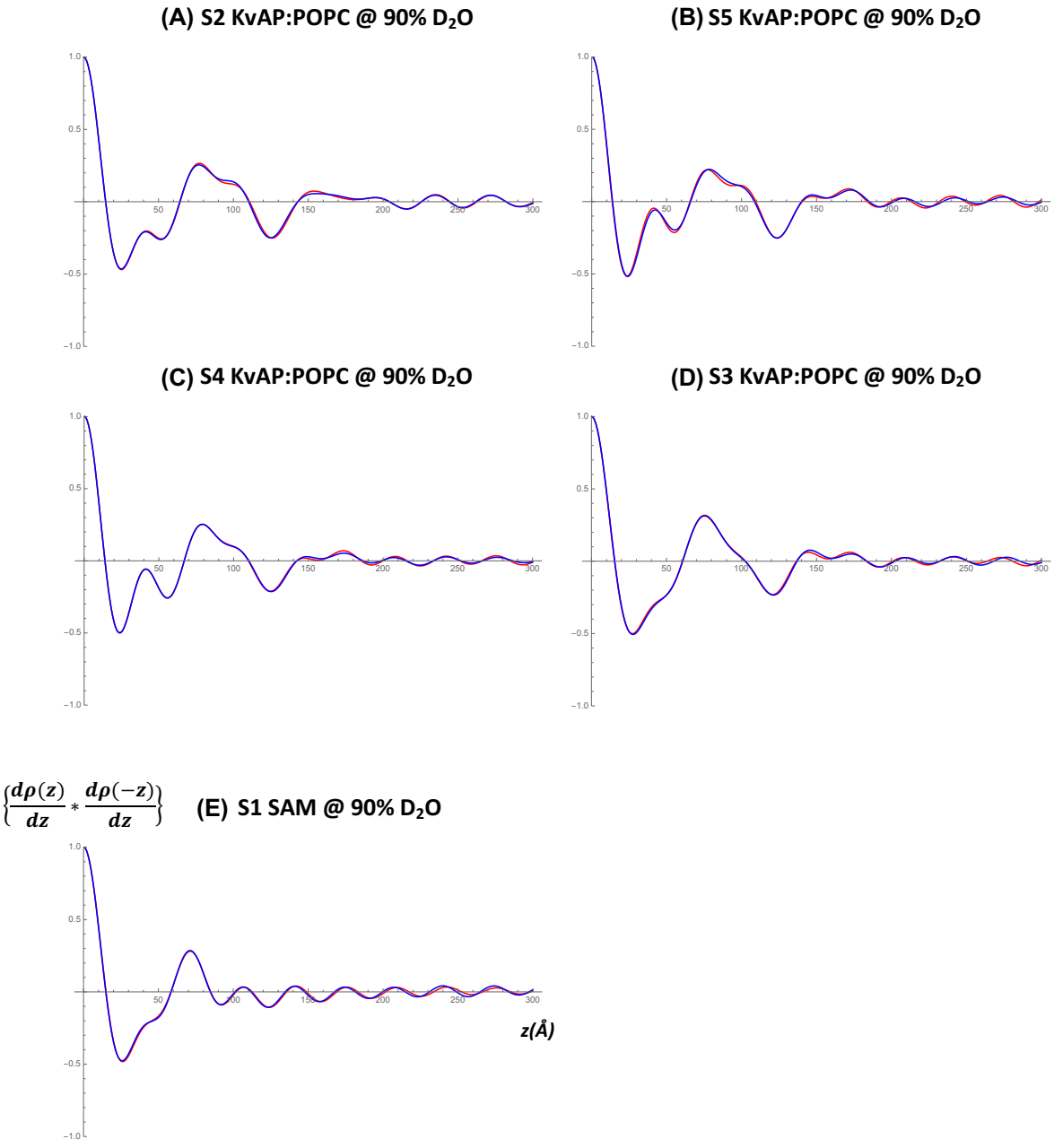
(A) S2 KvAP:POPC @ 90% D2O
(B) S5 KvAP:POPC @ 90% D2O
(C) S4 KvAP:POPC @ 90% D2O
(D) S3 KvAP:POPC @ 90% D2O
$\left\{\frac{d\rho(z)}{dz} * \frac{d\rho(-z)}{dz}\right\}$
(E) S1 SAM @ 90% D2O
z(Å)

Figure SM 3:

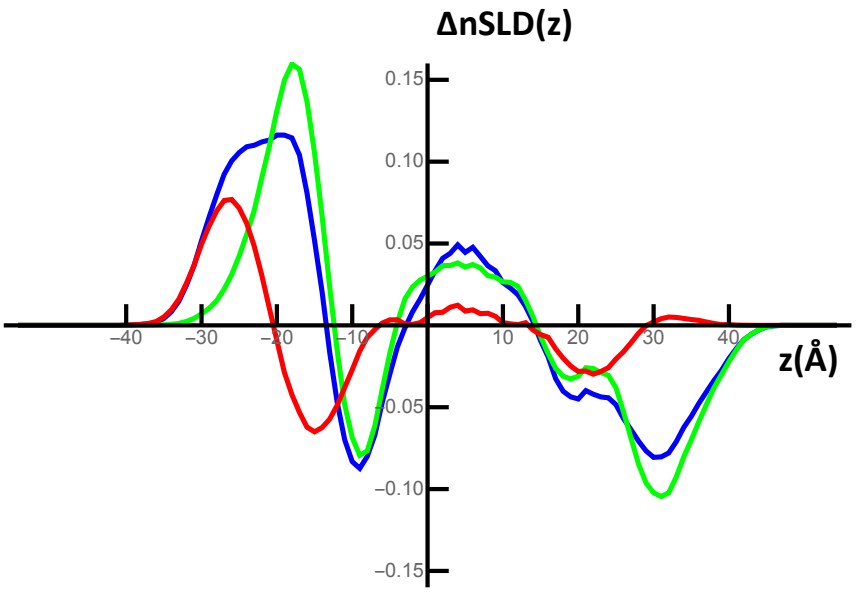

Figure SM 4:

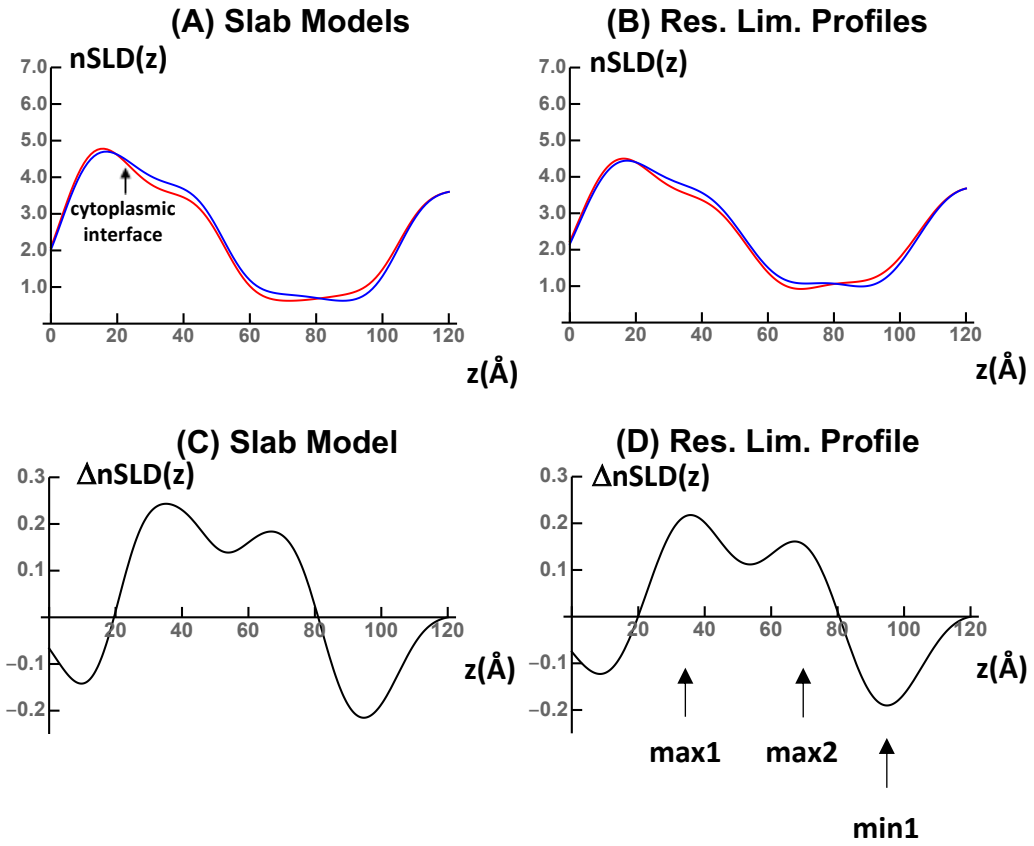

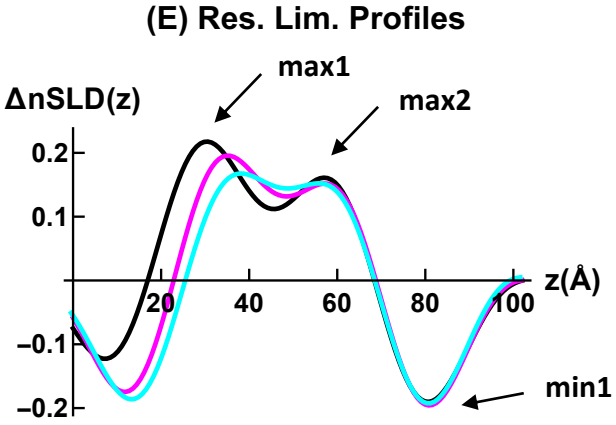

	Exp ΔnSLD KvAP	ΔnSLD Kv1.2/2.1	ΔnSLD Kv1.2	Resolution-limited ΔnSLD model 1	Resolution-limited ΔnSLD model 2	Resolution-limited ΔnSLD model 3
|Δ(max1-max2)|	28Å	28Å	20Å	27Å	22Å	18Å
|Δ(max1-min1)|	50Å	51Å	44Å	50Å	46Å	43Å